Surface curvature and basal hydraulic stress induce spatial bias in cell extrusion

Cheng-Kuang Huang[1,*,a)], Xianbin Yong[2,3,a)], David T. She[3,4], Chwee Teck Lim[1,2,3,4,†]

1 Mechanobiology Institute, National University of Singapore
2 Integrative Sciences and Engineering Programme, NUS Graduate School, National University of Singapore
3 Department of Biomedical Engineering, National University of Singapore
4 Institute for Health Innovation and Technology (iHealthtech), National University of Singapore

*** mbihc@nus.edu.sg**
† ctlim@nus.edu.sg

a) Authors of equal contribution

Summary

Cell extrusion is a coordinated biological process by which epithelial cells are removed from the epithelium without compromising the tissue's natural barrier function [1–3]. Cell extrusions not only occur when injuries or genetic mutations arise [4, 5], they also serve to maintain homeostatic cell numbers [6] and have been found to drive morphogenesis [1]. However, the effects of unique environmental settings—e.g., the complex geometric landscape and varying solute gradients in intestinal epithelia [2,7]—on cell extrusions are less explored. Here we show, using epithelial monolayers cultured on periodic wave substrates, that surface curvature can induce a spatial bias in cell extrusions, with cells more frequently extruding from the negatively curved valleys. Surprisingly, increasing media osmolarity significantly reduced this bias, and also overall extrusion numbers. Furthermore, basal fluid spaces were found smaller under monolayers in hyper-osmotic media compared to iso-osmotic conditions, and similarly smaller on the positively curved hills as compared to valleys. The latter corresponded with the measured inward pointing normal forces on the hills.

Remarkably, higher focal adhesion kinase (FAK) and Akt activation were observed in hyper-osmotically treated monolayers. Likewise, higher FAK activation was also observed in wave-hill residing cells. Our results show that surface curvature can play a modulating role in osmotically induced hydraulic stress levels, which act to disrupt focal adhesions and affect cell extrusions via FAK and the downstream Akt survival pathway. These findings highlight the fact that multiple environmental cues can synergistically influence cell extrusions. And an awareness of this will benefit our understanding of spatiotemporal preferences in cell extrusions seen in homeostasis, disease and development [8].

Results and Discussions

Characterization of 3D curved features

To explore the effects of surface curvature on cell extrusion, silicone substrates with cellular-scale wavy features were fabricated using a novel microfabrication procedure (see online methods and Extended Data Fig. 1 and 2). The features constitute a contiguous repeating array of approximately hemi-cylindrical valleys and hills. Three size conditions were included in this study; that is, waves with half-period dimensions of ∼200, ∼100, and ∼50 μm (Fig. 1a-c). By coating the surfaces with fluorescent collagen I (Extended Data Fig. 3a-c), the specific half-period dimensions were estimated to be 194.15 ± 2.9, 108.5 ± 0.5, and 56.6 ± 2.4 μm (mean ± SD, n = 6) (Extended Data Fig. 4). As support, these wave substrates were attached to 22 × 22 mm cover-glasses. After coating with collagen I, Madin-Darby Canine Kidney (MDCK) type II cells were seeded on to the substrates at densities of ∼250,000 cells/cm^2, in a 35 mm culture dish containing medium. In this way, a confluent monolayer is typically achieved after 24 hours.

When confluent with cells, the cover-glass supported substrates were transferred to stainless-steel cover-glass holders for imaging. To minimise medium evaporation, live-cell time-lapses were acquired on Biostations, which are microscopes with built-in isolated incubators. Figure 1d-f show representative phase contrast images of confluent MDCK monolayers on the 200, 100, and 50 μm waves, respectively.

Our waves are zero-Gaussian curvature surfaces, which can theoretically be mapped onto flat surfaces without distortion [9], so we developed a semi-automatic surface unwrapping algorithm for this (see online methods). This reduced the tedium in 3D image analysis by turning it into a 2D problem. Figure 1g-i show typical unwrapped fluorescent z-stacks of nuclei stained monolayers on 200, 100, and 50 μm

waves 24 hours after seeding. Using such nuclei images, the average cell densities prior to live-cell imaging were 2467 ± 282, 2563 ± 245 and 2509 ± 165 cells/mm^2 for 200, 100, and 50 μm waves, respectively (Fig. 1j, mean ± SD, n = 19, 25, 19 respectively). Comparisons of valley (cyan ROIs) and hill (magenta ROIs) densities yielded little differences (Fig. 1k).

Cells exhibit curvature dependent extrusions

In our live-cell imaging experiments, cells extruding from the monolayers on the 200, 100, and 50 μm waves were tracked for 24 hours (supplementary movie S1-S3) and then counted using an attention-gated residual U-Net trained with 3987 hand annotated examples (see online methods). The trained network was able to effectively differentiate actual extrusion events from floating debris (cyan highlights in Fig. 1i and supplementary movie S4; performance metrics in Extended Data Fig. 8c). This removed the need to manually count each image for extrusion events and allowed for more images to be analyzed, thereby increasing the sample size for the statistical tests. Figure 1m shows the determined extrusion rates, normalized against starting cell densities determined from phase-contrasts of planar regions. Two-way Anaylsis of Variance (ANOVA) was conducted at an alpha level of 0.05 to assess the effects of feature size (200, 100, and 50 μm) and curvature type (hills and valleys) on extrusion rates. As the interaction term was significant ($F(5,292) = 7.297$, $p = 1.849\times10^{-6}$), the simple main effects were examined. The differences between the two curvature types for each feature size were investigated, with alpha level set at $0.05/6 = 0.0083$ for each test. A significantly higher mean extrusion rate was found in the valleys compared to hills in both the 50 and 100 μm waves (Extended Data Fig. 5). Meanwhile, no significant difference was found for the same comparison on the 200 μm waves ($p = 0.561$), indicating that cells were unable to differentiate between convex, concave and planar surfaces at such scales.

For comparison, MDCK monolayers were also cultured on rectangular waves of similar size conditions (Extended Data Fig. 3d-f and supplementary movies S5-S7). As rectangular corners are essentially positively and negatively curved surfaces, extrusion sampling regions were defined to exclude the corners. Our results, shown in figure 1m (and table in Extended Data Fig. 5), revealed inconsistent valley-hill extrusion rate differences in cell monolayers on the rectangular waves: no difference on the 200 and 50 μm rectangular waves, but slightly higher valley extrusion rates on the 100 μm rectangular waves. Spatially resolving the cell extrusions (Fig. 1n) revealed an increasing trend from pattern centre to corner, indicating that curvature effects can extend beyond its immediate location, contributing to the inconsistencies

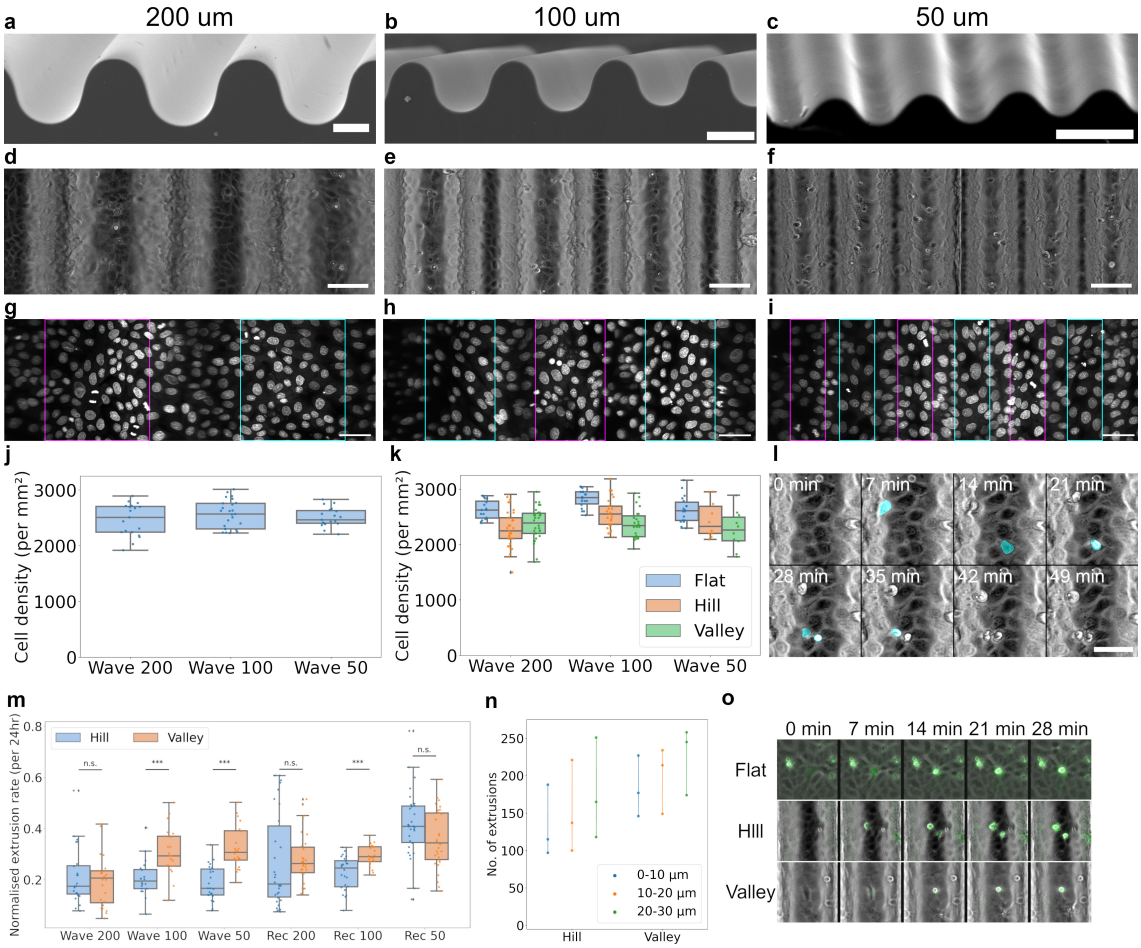

Figure 1: **Epithelial monolayers exhibit higher cell extrusion rates in negatively curved valleys of cylindrical wave substrates. a-c**, SEM images of 200, 100 and 50 μm waves. Scale-bar: 100 μm. **d-f**, phase contrast images of confluent MDCK monolayers on 200, 100 and 50 μm waves, 24 hours after seeding. **g-i**, surface unwrapped fluorescent z-stacks of Hoechst stained MDCKs on 200, 100 and 50 μm waves. Hills: cyan boxes and Valleys: magenta boxes. **j**, boxplot of overall cell densities, determined from nuclei staining, across wave dimensions at the initial time point. **k**, cell densities in **j** plotted according to curvature type. **i**, time-lapse excerpt demonstrating extrusion event registration (cyan objects) using our trained neural network. **m**, boxplot of extrusion events registered over 24 hours, on 200, 100 and 50 μm cylindrical waves, and on 200, 100 and 50 μm rectangular waves for comparison. **n**, boxplot of 100 μm rectangular wave extrusions plotted against distance from pattern centers grouped into 3 bins. **o**, multi-channel time-lapse excerpts of cells incubated with activated caspase 3/7 reporter (false green over phase contrast), on flat, hill and valley regions of an 100 μm wave: dying cells are accompanied by fluorescence. Scale-bars (unless otherwise stated): 50 μm. *p $<$ 0.05; **p $<$ 0.01; ***p $<$ 0.001.

observed.

Epithelial cell extrusions can either be apoptotic, or they can be live extrusions in response to extreme crowding [6]. In our case, live-cell imaging with the activated Caspase 3/7 reporter substrate, CellEvent™ (Fig. 1o and supplementary movie S8), show that almost all extrusion events, irrespective of location, were accompanied by fluorescence; i.e., they are dying. Evidently, MDCK extrusions seen in our studies are apoptotic, and the valley-hill extrusion rate differences were not a result of curvature promoting one extrusion type over the other.

Basal hydraulic stress underlies cell extrusions

Besides valley-hill differential extrusion rates, we also observed a preferential appearance of fluid-filled domes in the valleys at longer times (>48 hours) (Fig. 2a and supplementary movie S9). As confluent epithelial monolayers function like semipermeable membranes [10], this separation of the cell monolayer from the substrate indicated an increasing basal hydraulic stress due to osmotic effects. Specifically, over time, water will tend to move into the basolateral compartments with rising sodium concentrations there due to cellular active ion pumping [11].

We thus asked if hydraulic stress could be underlying the extrusion differences observed at earlier time points. To test this, we subjected MDCKs on 100 μm waves to media of various osmolarities prior to imaging. To eliminate non-specific effects from the solutes, three independent hyper-osmotic conditions were employed in the following extrusion studies—normal media containing either 1 % DMSO, 4.1 wt. % sucrose, or 0.4 wt. % NaCl (supplementary movies S10-12). For comparison, a hypo-osmotic condition prepared by adding 25 % water to normal media was also included (supplementary movies S13). The osmolarities calculated from measured osmolalities were 279.3 ± 3.8, 418.6 ± 3.5, 403.6 ± 3.8, 406.3 ± 1.5 and 214.6 ± 4.0 mOsm/L (mean ± SD, n = 3) for control, DMSO, sucrose, NaCl and water treatments, respectively.

Figure 2b shows the determined extrusion rates from our osmolarity perturbations. Two-way ANOVA was then performed at an alpha level of 0.05 to assess the effects of osmolarity (control, sucrose, DMSO, NaCl and water) and curvature type (flat, valleys and hills) on extrusion rates (see table in Extended Data Fig. 6). A significant interaction term was observed ($F(8,362) = 6.136$, $p = 1.989\times10^{-7}$). Comparing the simple effects for each curvature, adjusting osmolarity had a significant effect on extrusion rates (flats: $F(4,74) = 60.805$, $p = 1.200\times10^{-22}$; hills: $F(4,144) = 70.846$, $p = 4.689\times10^{-33}$; valleys: $F(4,144) = 138.930$, $p = 2.150\times10^{-48}$). Strikingly, by simply increasing the osmolarity of the culture media, we were able to significantly reduce

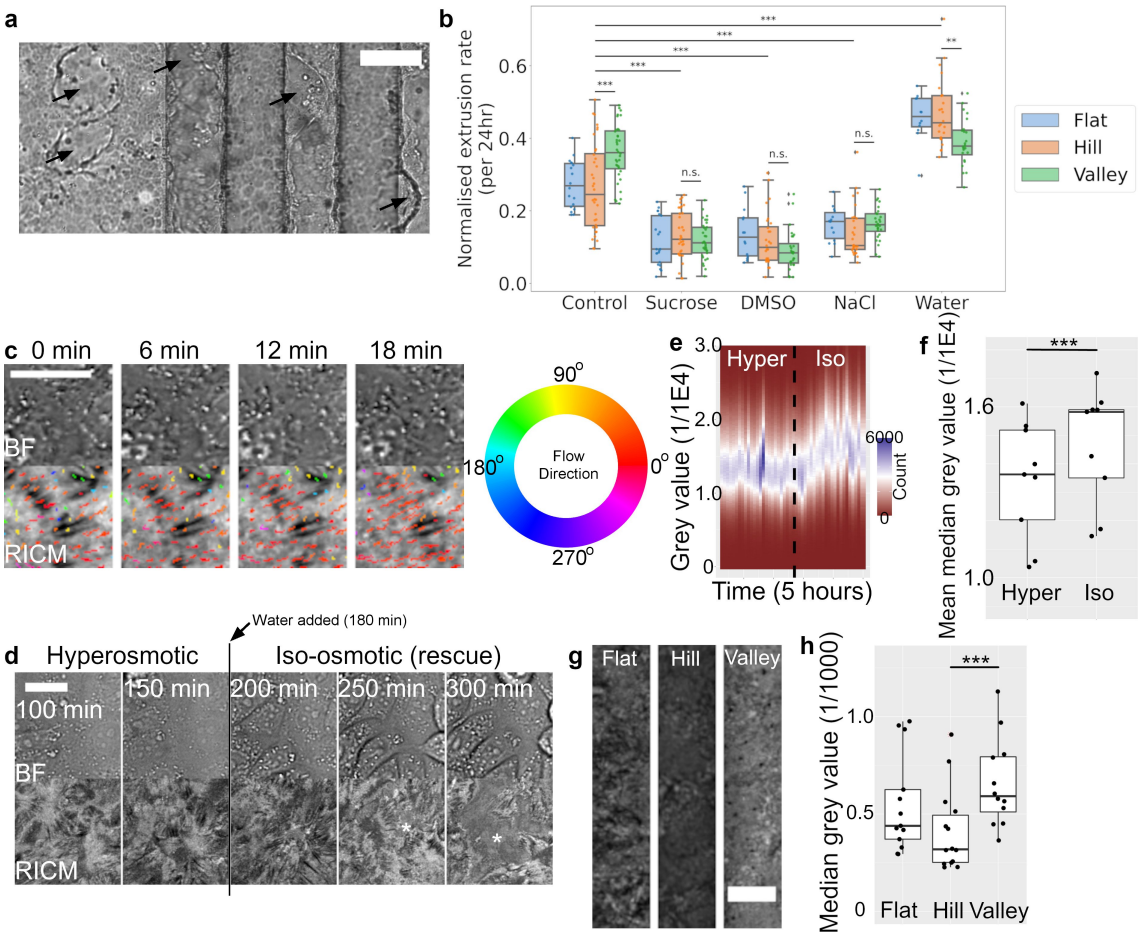

Figure 2: **Osmosis induced basal hydraulic stress is linked to cell extrusions.** **a**, confluent MDCK II monolayers form fluid-filled domes (arrows) in wave valleys when cultured for over 48 hours. Scale-bar: 100 μm. **b**, boxplot of extrusion events over 24 hours on 100 μm cylindrical waves, with monolayers subjected to osmolarity perturbations that included the addition of 1 % DMSO, 4.1 wt. % sucrose, 0.4 wt. % NaCl, and 25 % water. **c**, bright-field/RICM time-lapse excepts showing dynamic basal fluid spaces whose motion (direction encoded colored paths) corresponded with the direction of focal adhesion (dark streaks) disassembly. **d**, bright-field/RICM time-lapse excepts showing the accumulation of basal fluid (asterisks) when iso-osmolarity was reinstated (at 180 min) in hyper-osmotically pre-conditioned monolayers. **e**, plot of the image histograms against time showing an increase in grey values as iso-osmolarity was restored, indicating a general increase in basal-to-substrate separations with decreasing apical media osmolarity. **f**, boxplot of histogram median grey values from **e** averaged separately over the duration of hyper- and iso-osmolarity treatments. **g**, representative max-projected RICM z-stacks of flat, hill and valley regions. **h**, boxplot of histogram median grey values from images such as in **g**. **c,d,g** scale-bars: 20 μm. *p $<$ 0.05; **p $<$ 0.01; ***p $<$ 0.001.

the overall cell extrusion rates compared to the control (Extended Data Fig. 6). Moreover, the treatments also resulted in reduced valley-hill extrusion rate differences (Extended Data Fig. 6). Specifically, no significant differences in extrusion rates between the curvature types were detected for all three hyper-osmotic treatments (sucrose: $F(2,84) = 0.740$, $p = 0.480$; DMSO: $F(2,67) = 2.961$, $p = 0.059$; NaCl: $F(2,67) = 1.097$, $p = 0.340$).

Consistent with the effects of hyper-osmolarity, diluting media with extra 25 % water to reduce osmolarity resulted in an increase in overall extrusion rates (Fig. 2b, Extended Data Fig. 6)). Interestingly, valley extrusions did not increase accordingly to maintain the original difference, and led to a flipped valley-hill extrusion difference ($F(2,57) = 7.594$, $p = 1.192\times10^{-3}$, Extended Data Fig. 6). This observation suggests a boundary limit to increasing extrusions. Indeed, given a specific proliferation rate, extrusion rates cannot increase indefinitely without compromising monolayer integrity; the latter itself a prerequisite for the cell extrusion phenomenon.

As cell adhesions give way to hydraulic stress, the accumulation of fluid is inevitable. To verify the existence of such nascent fluid spaces beneath MDCK monolayers, reflection interference contrast microscopy (RICM) was employed. Relying on the interference of reflected light from the substrate and the cell membrane, the method produces image intensities that are sensitively coupled to basal membrane distances from the substrate [12–14]. In particular, it has been verified that attached cellular regions (e.g., focal adhesions) appear the darkest, with intensities increasing with basal separation [12, 13]. Our RICM time-lapse observations, represented in sequence excerpts in figure 2c (supplementary movie S14), do reveal numerous continuously moving bright regions (i.e., fluid spaces) under MDCK monolayers on planar substrates. Interestingly, optical flow analysis [15] performed on the sequences showed a qualitative correspondence between the directions of the fluid motion (flow paths in figure) and focal adhesion disassembly (dark streaks disappearance). To show that changing osmolarity was sufficient in tuning these basal separations, we tracked variations in the RICM intensities of monolayers pre-conditioned in hyper-osmotic 4.1 wt. % sucrose media, followed by the addition of water to reinstate iso-osmolarity (Fig. 2d and supplementary movie S15). Evidently, as osmolarity was raised back to normal, fluid-filled spaces (asterisks in figure) begin to develop and eventually span underneath several cells. Moreover, minimum grey value matched histograms of each time-frames plotted against time (Fig. 2e) show the central tendencies of images shifting towards higher intensities upon raising osmolarity. From the principles of RICM, the latter effect signifies that basal cell membranes are moving further away from the substrate in general. Figure 2f shows the boxplot of average histogram me-

dians before and after raising osmolarity. Paired sample t-test revealed a significant difference between the two conditions ($t(8) = 6.63$, $p = 1.65\times10^{-4}$). So hydraulic stress appears to be correlated with cell extrusion rates on planar surfaces. To show hydraulic stress also correlates with extrusion rate differences seen on curved surfaces, we next compared RICM images of MDCK monolayers on the various curvature types of 100 μm wave substrates. As demonstrated in figure 2g, minimum grey value matched RICM z-stack maximum projections do reveal subtle intensity differences, with contrast appearing the darkest on the hills and brightest in the valleys. Indeed, as shown in figure 2h, valley image median grey values are generally higher than those of the hills and flats. Student's t-test revealed a significant difference between the valley and hill median grey values ($t(22.8) = -2.84$, $p = 0.009$). Similarly then, like monolayers in hyper-osmotic media, we can assume that monolayers are more closely apposed to the surface on the hills, and less so in the valleys.

Both the osmolarity and surface curvature RICM studies showed us that smaller basal-to-substrate separations translate to lower extrusion rates. While in hyper-osmotic treatments this reduced separation is achieved through drawing water from the basal side by osmosis, it is unlikely that neighboring valley and hill regions in the same medium are subjected to differing osmolarities. Instead, judging from geometry, if epithelial forces pointed down into the substrates in the hill regions, its smaller basal-to-substrate separation can be accounted for. These forces will effectively work against hydraulic stress to promote adhesion formation and persistence. In support of this, nuclei are readily observed deformed against the surface on the wave hills (figure 3a). We subsequently quantified epithelial force distributions over our wave substrates using a finite-element 3D force microscopy (see online methods). Figure 3b shows a representative unwrapped monolayer normal force distribution on a 100 μm wave. On the 100 μm waves, the magnitudes of the normal forces varied consistently over the waves, with monolayers on the hills producing larger normal forces. Interestingly, this effect appears to be curvature dependent (Fig. 3c), with 50 μm waves showing the greatest range of magnitudes while the 200 μm structures having an approximately even distribution of force magnitudes along the curved structure (50 μm: [1.138, 10.972]; 100 μm: [1.116, 7.725]; and 200 μm: [1.955, 4.356] nN/μm^2). The direction of the normal forces, on the other hand, are in general pointing into the substrate on the hills for both the 50 and 100 μm waves. And this normal component strength decreases as we move away from the hill tops, flipping to outward pointing at the valley-hill interface (figure 3d). Again, the 200 μm did not exhibit any clear curvature dependent directional patterns.

To further support that hydraulic stress contributed to the cell extrusions ob-

served, rather than some cryptic effects of changing osmolarity, we tracked MDCK monolayers cultured on hydrogel substrates in iso-osmotic medium. Being water and solute permeable materials, hydrogels can buffer against drastic increase in solute concentrations, thereby lowering osmosis induced hydraulic stress. To eliminate the possibility that any extrusion differences were due to hydrogels being a much softer material (∼30 kPA [16]), MDCK monolayers cultured on silicone substrates of similar stiffness (∼25 kPA [17]) were also tracked (Fig. 3e). Figures 3f shows that the extrusion rate differences between the materials were significant ($F(2,64) = 53.343$, $p = 2.330\times10^{-14}$). Compared to monolayers on stiff silicone substrates, monolayers on polyacrylamide (PAM) gels produced fewer extrusions over 24 hours (-0.168, Welch's $t(20.9) = -6.316$, $p = 2.72\times10^{-6}$, 95% CI Cohen d = [-0.953, -3.157]; supplementary movie S16). Furthermore, monolayers on soft silicone substrates actually showed higher extrusion rates than their counterparts on stiff silicones (0.096, Welch's $t(38.9) = 4.801$, $p = 2.349\times10^{-5}$, 95% CI Cohen d = [0.632, 1.843]). Notably, as easily inferred from the images, monolayers on PAM hydrogels typically reached higher cell densities; this, we presume, is due to the fewer extrusions and therefore more dividing cells.

As cell adhesion is intimately related to cell survival [18], our experimental evidences suggest that hydraulic stress may be inducing the apoptotic cell extrusions by antagonizing cell-substrate adhesions. A likely mechanism is through the reduction of focal adhesion kinase (FAK) auto-phosphorylation at tyrosine residue 397, which ultimately leads to a reduced activation of the Akt survival cascade [19]. From this, we predicted that the pro-survival effects of hyper-osmolarity would be abolished if FAK inhibitors were introduced together. We tested this by adding 3 μM of specific FAK inhibitor at tyr397 (FAKI14) to hyper-osmotic 4.1 wt. % sucrose media—sucrose being the most inert of the 3 hyper-osmotic treatments to cells—and imaged for 24 hours (supplementary movie S17).

As predicted, higher extrusion rates were seen when FAKI14 inhibitor was added, as compared to the sucrose treatment alone, in all three curvatures types (Fig. 4a, Extended Data Fig. 7). In addition, the extrusion rates between the FAKI14 treatment were similar to that in the control for both the flat and valley regions (Extended Data Fig. 7). Although the hill region differences in the two treatments were statistically significant, the difference is clearly smaller than the hill region differences between control and sucrose alone (Extended Data Fig. 7). The valley-hill extrusion rate difference was also restored in the FAKI14 treatment despite the higher osmolarity (Extended Data Fig. 7). Further increasing the FAKI14 concentrations to 6 μM induced massive cell deaths, and led to monolayer disintegration (Fig. 4b

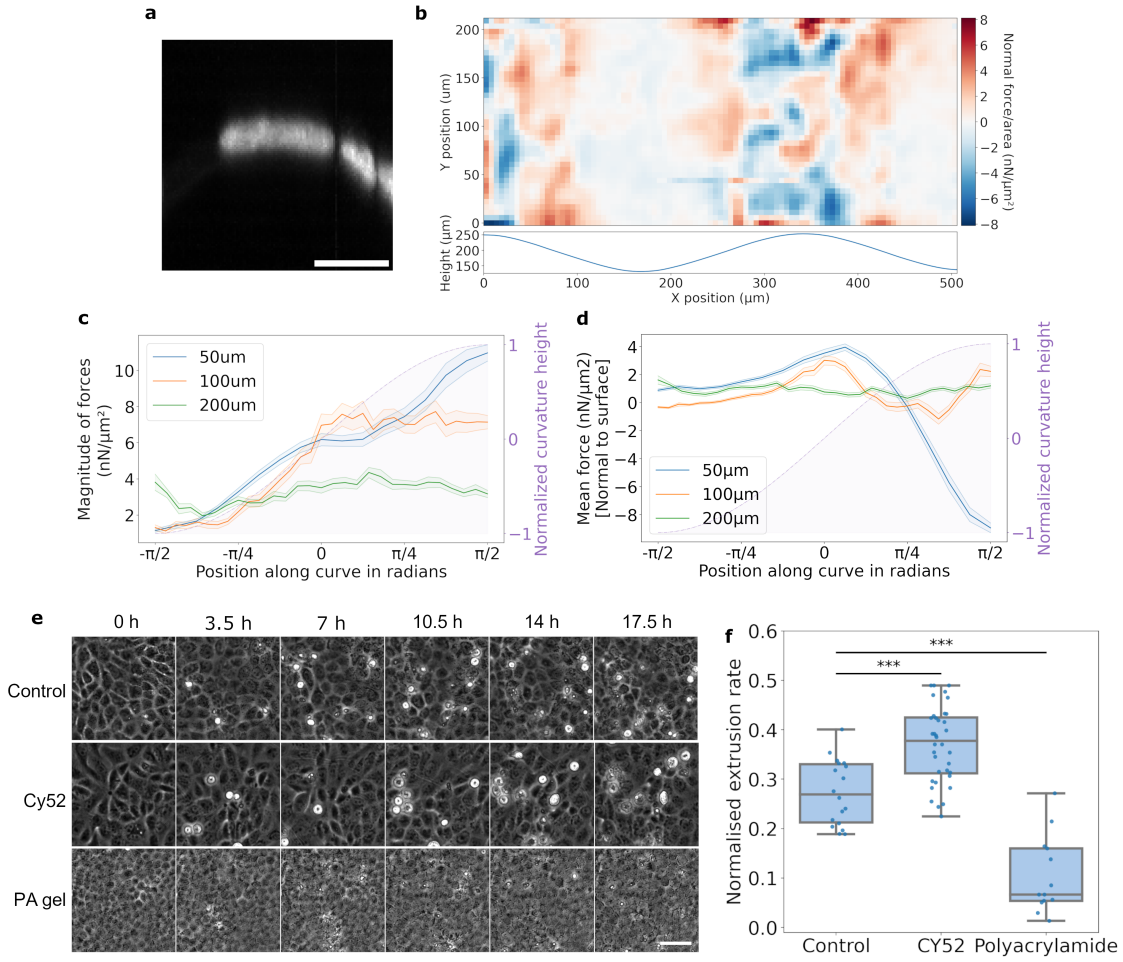

Figure 3: **Surface curvature induces monolayer force symmetry breaking and mass transferable hydrogel substrates effective in reducing cell extrusions.** **a**, fluorescence nuclei side profiles show clear deformation against substrate on wave hills (scale bar: 10 μm). **b**, 3D force microscopy reconstructed monolayer normal force component distribution on a 100 μm wave, with wave profile shown below. **c**, graph showing the magnitude of calculated forces along the curved profile (purple shaded region). **d**, normal force vectors along the curved profile (purple shaded region). **e**, time-lapse excerpts showing cell extrusion accumulation on stiff PDMS (control), and on soft silicone and PAM hydrogel of similar stiffness (scale bar: 50 μm). **f**, boxplot showing the cell extrusion rates from the 3 substrates in **e**. *$p < 0.05$; **$p < 0.01$; ***$p < 0.001$.

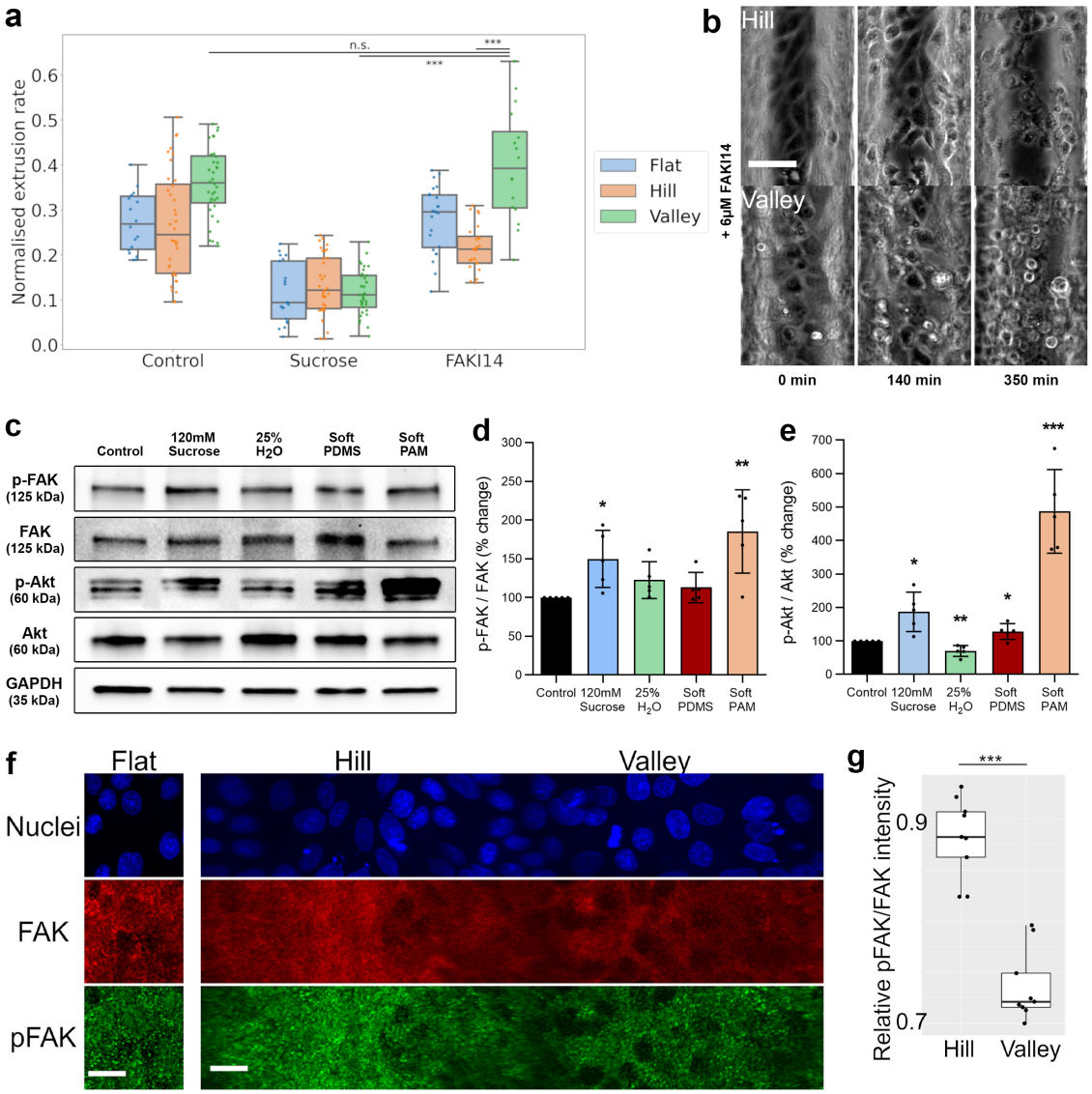

Figure 4: **Modulation of basal hydraulic stress through media osmolarity and substrate mass transferability regulate cell extrusion via FAK-Akt pathway a**, cell extrusion rates on 100 μm waves in normal, 4.1 wt. % sucrose, and 4.1 wt. % sucrose + 3 μM FAKI14 media. **b**, bright-field time-lapse excerpts showing massive cell death leading to compromised monolayers with 6 μM FAKI14. Scale-bar: 50 μm. **c**, representative immunoblots of focal adhesion kinase (FAK) and Akt proteins in MDCK cells subjected to treatments that lead to varying basal hydraulic stresses; namely, hyper- (4.1 wt. % sucrose), hypo- (25 % H_2O), iso-osmotic (control) condition, iso-osmotic with reduced substrate stiffness (soft PDMS) and iso-osmotic with water/solute permeable soft PAM hydrogel for a period of 24 hr. **d, e**, quantification of the relative expression levels of phosphorylated-FAK (Tyr397) as a ratio of p-FAK to total FAK and phosphorylated-Akt (Ser473) as a ratio of p-Akt to total Akt, respectively. GAPDH was used as loading control. Data are presented as mean ± SD, n = 5 cultures. **f**, fluorescence images of cell nuclei (false blue), FAK (false red), and p-FAK at tyr397 (false green) on flat, hill and valley; the hill and valley images were unwrapped from 3D stacks. Scale-bar: 20 μm. **g**, boxplot of normalized p-FAK/FAK intensities from hill and valley cells. *$p < 0.05$; **$p < 0.01$; ***$p < 0.001$.

and supplementary movie S18).

To show that modulation of osmolarity affected Akt signalling in a FAK dependent manner, we have immunoblotted (Fig. 4c) and quantified the protein expression levels of MDCK monolayers cultured in hyper-osmotic, hypo-osmotic, and iso-osmotic media, and, for comparison, also on soft silicones and PAM hydrogels. As shown in Fig. 4d, e, monolayers in media supplemented with 120mM sucrose (hyper-osmotic) showed significantly higher levels of phosphorylated-FAK ($P = 0.0167$) and phosphorylated-Akt ($P = 0.0108$) compared to those in iso-osmotic control group. These findings agree with previous observation that higher activated Akt levels in epithelial cells subjected to hyper-osmotic treatment [20]. Conversely, the levels of p-Akt was significantly reduced ($P = 0.0033$) in hypo-osmotic group, and resulted in significantly elevated extrusion rate as compared to iso-osmotic control group (Fig. 2b). Interestingly, the level of p-FAK was not affected by the augmented hydraulic stress (Fig. 4d). We have also noted that cells cultured on PAM hydrogels revealed significantly elevated levels of both p-FAK ($P = 0.0076$) and p-Akt ($P = 0.0001$) compared to those on stiff silicone in iso-osmotic control group, and to our surprise, the extent of Akt activation is even more prominent (2.5-fold increment, $P = 0.0013$) than cells in hyper-osmotic media. Collectively, our findings indicated that monolayers maintained in reduced hydraulic stress (hyper-osmotic media and soft PAM) expressed higher levels of FAK and Akt activation, leading to up-regulated pro-survival signal which ultimately resulted in lower apoptotic cell extrusions.

To show that the same mechanism applies to valley-hill cell extrusion rate differences, we visualized p-FAK and FAK on 100 μm waves (Fig. 4d). Prior normalizations were applied to the images (see online methods) to compare the relative activation p-FAK/FAK between hill and valley monolayers. The ratio of p-FAK/FAK median intensities are shown in figure 4e. And in accordance with our observed higher valley extrusion rates, valley cells indeed exhibited lower pFAK/FAK ratios compared to hill cells ($t(16) = 8.33$, $p = 3.27\times10^{-7}$).

In conclusion, in this investigation, we have shown that hydraulic stress can induce epithelial cell extrusion by disrupting cell adhesions, and subsequently inhibiting downstream Akt survival signals (Fig. 5a, b). Moreover, an emergent spatial bias in cell extrusion is elicited when hydraulic stress is coupled with the curvature induced symmetry breaking of epithelial forces. Specifically, positive curvature induces a pro-survival, inward pointing normal force, on convex surfaces that favors cell adhesions. On the other hand, negative curvature on convex surfaces elicits a pro-death, outward pointing force, that work with hydraulic stress to antagonize cell adhesions (Fig. 5c). Recent developments have shown that curved surfaces can direct

intestinal epithelial cell differentiation through shaping morphogen gradients [21] and influence intracellular YAP/TAZ localization [22]. Our findings now reveal that surface curvature can also spatially bias cell extrusions. This has significant *in vivo* implications as such selective removal of cells can easily lead to segregated populations of differentiated cells, and could well be employed during morphogenesis. Moreover, the net effect of cellular forces on the positive hills is essentially reverse osmosis, thus it will be interesting to explore in future whether the surface curvature induced epithelial force symmetry breaking is utilized in the body to regulate water transport and solute concentrations during homeostasis.

Acknowledgements

We would like to thank the National University of Singapore (NUS) Mechanobiology Institute for the support, facilities and resources provided during the course of this work. We would also like to thank Dr. Natalia Veronica and Dr. Wan Sia Heng at the Department of Pharmacy, NUS, for assisting in the measurement of the media osmolality, and our colleague Dr. Chii Jou Chan for his suggestions and advice on the paper. X.Y. is supported by the Integrative Sciences and Engineering Programme Scholarship from the NUS Graduate School; National University of Singapore.

Funding Statement

This work was supported by a Human Frontier Science Program Research Grant [grant number RGP0038/2018].

Author Contributions

C.K.H. designed the method of fabrication for the 3D structures. C.K.H. and X.Y fabricated the 3D structures, performed the experiments and developed the tools required for the quantification of the experimental results. D.S. performed the western blots and determined the protein levels for the various treatments. C.K.H, X.Y. and D.S. contributed to the interpretation of results and writing of the manuscript. C.T.L supervised and provided critical feedback throughout the various stages of the project and guided the shaping of the manuscript. All authors gave final approval for publication and agree to be held accountable for the work performed therein.

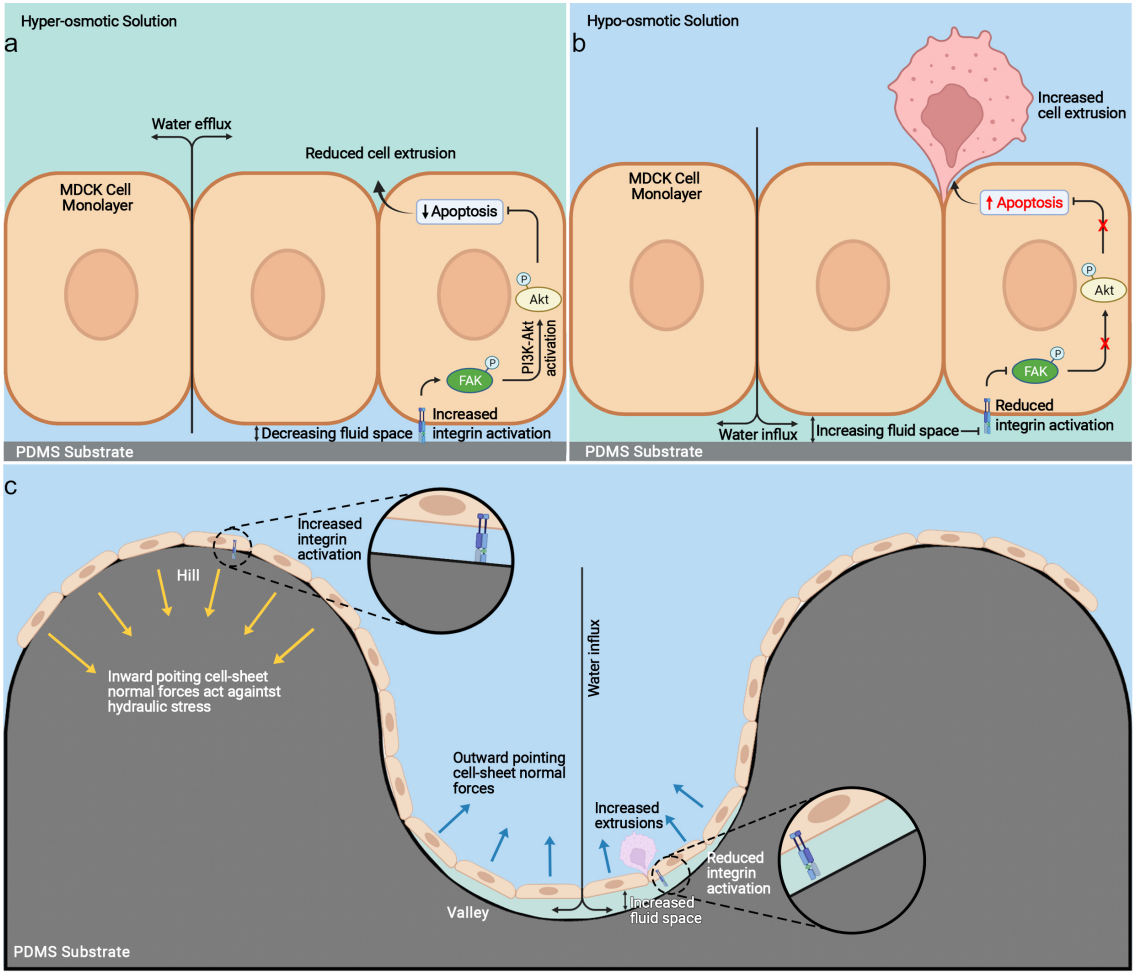

Figure 5: **Schematic explanation of basal hydraulic-stress induced epithelial extrusion and how surface curvature induced monolayer force symmetry breaking leads to differential extrusion rates. a**, hyper-osmotic media causes water to be drawn out of the basal space, reducing the membrane-surface distance. This reduces fluid pressure acting on the focal adhesions and further promotes the likelihood of adhesions forming. Increasing adhesion numbers, and therefore FAK autophophorylation at tyrosine residue 397, lead to an up-regulation PI3K/Akt signals, which ultimately boost cell survival. **b**, situation is reversed in hypo-osmotic media. This time water tends to accumulate in the basal space, increasing fluid pressure and over time disrupts adhesions and reduces chances of new ones forming. **c**, surface curvature induces a monolayer force symmetry breaking. On the hills the inward-pointing normal force components help maintain cell adhesions by acting against hydraulic stress. The situation is reversed in the valleys, with outward-pointing forces furthering the disruption of adhesions. Together, these lead to spatially biased cell survival and extrusion over curved landscapes.

Competing interests

We declare that we have no competing interests.

Ethics

This article does not present research with ethical considerations.

Materials and Methods (Online)

Microfabrication of periodic cylindrical wave structures

The microfabrication of our hemi-cylindrical wave substrates is, in principle, achieved by first manipulating and fusing multiple glass rods to produce an arrayed template. Then, through a series of moulding and surface processing, this template is ultimately replicated in a robust monolithic resin format that can be repeatedly moulded with silicone elastomer, or other soft biocompatible material, to create curved surfaces for 3D tissue culture. It is worth noting that, although the idea of molding cylindrical structures to create curved substrates is not new [23], our use of tight tolerance glass rods facilitates the production of very smooth surfaces. This is in contrast with methods that use metal wires [24] which, with their considerable machining defects, may contribute to spurious cellular responses. Furthermore, as will be described shortly, by selectively removing every other rod from the array, we were able to achieve a contiguous wavy landscape that is symmetric in the dimensions of the concave and convex regions.

Extended data figure 1 schematically illustrates in detail the microfabrication procedures involved in producing our cylindrical wave structures. There are essentially 4 major steps in our pipeline:

Step 1. (Extended Data Fig. 1a) The first goal is to produce an array of tightly packed uniform glass rods (100 & 200 μm dia., Hilgenberg GmbH, Germany) fixed in place with an UV curable optical adhesive—the Norland Optical Adhesive 73 (NOA73, Norland Products Inc., UK). To accomplish this, a glass slide is first pre-treated with Rain-X (800002250, ITW Global Brands, US) according to the manufacture's instructions; this is to facilitate NOA73 lift-off later in the procedure. Then, a thin layer of NOA73 is smeared on to the slide followed by the one-by-one placement of glass rods. The quantity of rods will determine the number of periods produced: for example, 10 rods will produce a pattern with 5 periods. With the rods laid down, using a sharp needle under an optical microscope, the rods are pushed

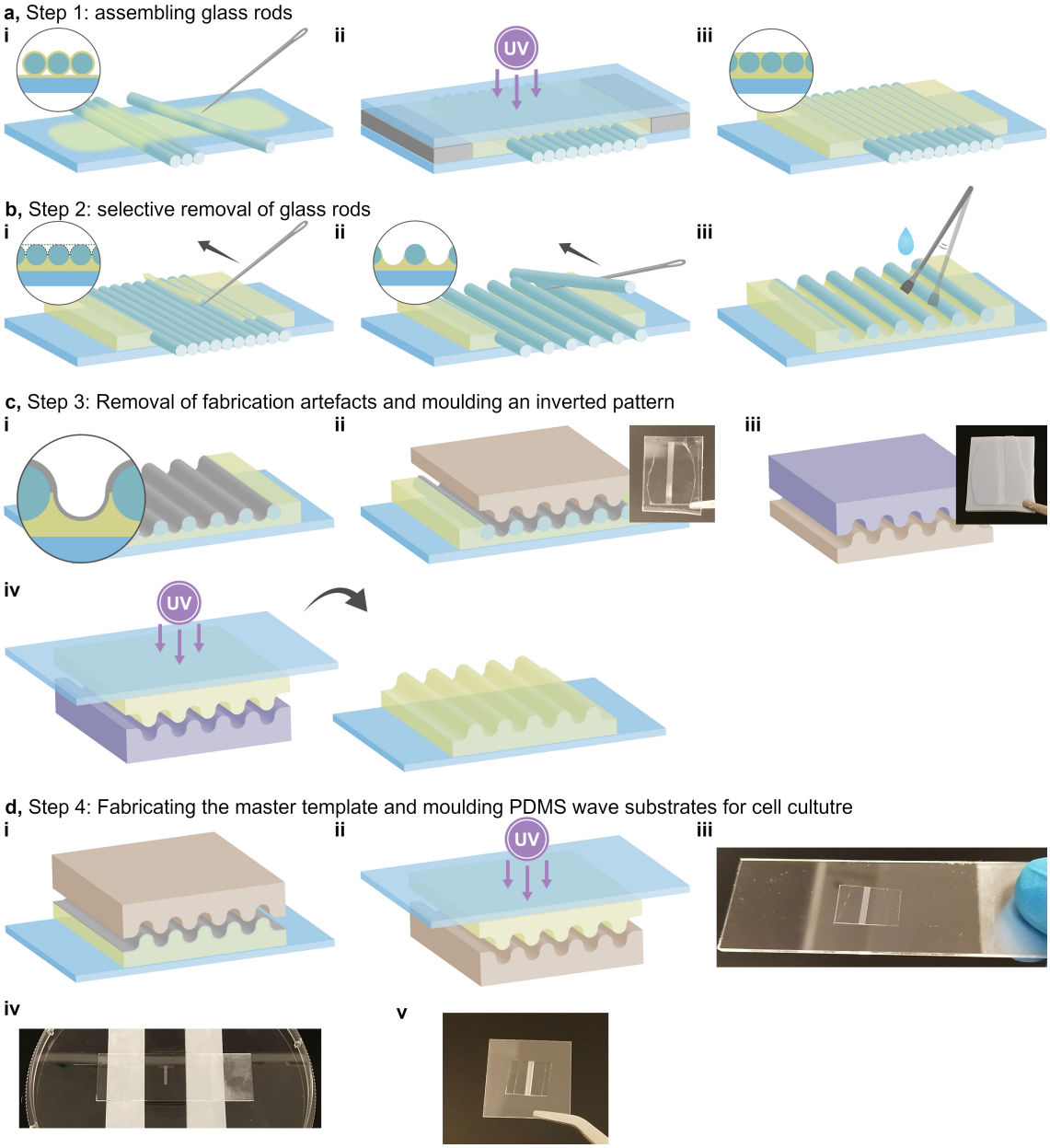

Extended Data Figure 1: **Schematics of the microfabrication of smooth periodic cylindrical wave substrates using glass rods and iterative molding processes.**

tightly together, all the while avoiding debris trapping in-between (Extended Data Fig. 1a i). Surface tension from the minimal amount of NOA73 will aid in holding the rods together here. Note that having excessive NOA73 will cause the rods to drift apart instead. To hold the rods in place, the array is then pre-fixed under UV illumination for 1 minutes at 25 % power in a UV-KUB 9" (KLOE, France). After this procedure, two spacers of ∼1 mm thick are placed either side of the array (Extended Data Fig. 1a ii), and additional NOA73 is poured over the array sufficiently covering it. A second glass slide is placed on top, propped by the spacers, sandwiching the whole construct; there should be enough NOA73 to fill the gap. Again, the NOA73 is cured under UV, this time for 2 minutes at 25 % power. Once the resin has cured, the sandwich construct is pried apart, with separation occurring at the Rain-X treated slide (Extended Data Fig. 1a iii).

Step 2. (Extended Data Fig. 1b) With the NOA73 embedded glass rods, we now remove every second rod in the array to create a wave structure symmetric in its concave and convex curvatures. To do this easily, residual NOA73 on the top side of the array is first cleared away. Specifically, a sharp needle is pushed along the grooves between the rods, from one edge to the other (Extended Data Fig. 1b i), lifting off resin from these regions. Then, with the same needle, every other rod is gently pried from the edge by wedging the needle tip under the rods. To prevent breaking the delicate rods, rather than lifting them off vertically, the needle is ran underneath the length of the rods (Extended Data Fig. 1b ii). It should be emphasized that goggles should be worn throughout this procedure in case rods break and flick off. A pool of water over the pattern can be added for protection; it buffers the sudden release of elastic energy. After creating the wave structure, the whole template is gently cleaned using a stiff paint brush, in ethanol followed by water, to remove NOA73 debris.

Step 3. (Extended Data Fig. 1c) In the previous step, due to the finite thickness of the resin, removing rods will unavoidably create a seam along the junction of the rods (Extended Data Fig. 1c i inset). To remove these seams, the glass rod wave template is spin coated with a layer of polystyrene cement (3527C, Testors, US) at 1500 RPM for 10 minutes (WS-400BZ-SNPP/LITE, Laurell Technologies, UK). This extra coat of film will however reduce the concave region's dimensions while increasing that of the convex region's. We can regain some of the dimensional symmetry by inverting the template followed by a second polystyrene spin coat. To perform the inversion, two part silicone elastomer, polydimethylsiloxane (PDMS sylgard 184, Dow Inc., US), with cross-linker and monomer mixed in a 1:10 weight ratio, is first moulded against the original polystyrene-coated template (Extended

Data Fig. 1c ii). We then create a negative of this PDMS mould by casting against it a second two-part silicone elastomer (Wirosil, BEGO Canada Inc, CA) (Extended Data Fig. 1c iii). To prevent fusion of the silicones, the PDMS mould was pre-coated with 1 % bovine serum albumin (BSA, A9647-50G, Sigma-Aldrich) reconstituted in Milli-Q water: the deposited BSA acts effectively as a de-moulding layer. The inverted wave template can then be derived by UV curing some NOA73 sandwiched between the Wirosil silicone mould and a glass slide (Extended Data Fig. 1c iv). The resulting inverted NOA73 template is subsequently spin coated with a second coat of polystyrene, balancing out the aforementioned dimensional deviations. This substrate also constitutes our master wave template.

Step 4. (Extended Data Fig. 1d) The final step of our procedure is to produce multiple resin clones of the master template. These clones, by virtue of parallel fabrication, will facilitate the scale-up production of wave structures for cell culture. For this, we first create a PDMS mould from the master template (Extended Data Fig. 1d i). Then, using this mould, we repeatedly cast NOA73 against it, deriving multiple monolithic NOA73 clones on glass slides (Extended Data Fig. 1d ii and iii). The clones are subsequently baked at 80 °C for 24 hours before they are used to cast PDMS substrates for cell culture: without baking to inactivate adhesion promoters, NOA73 inhibits PDMS curing. Thereafter, to fabricate wave substrates for cell culture, PDMS is poured onto each clone template and pressed against a polystyrene slab (a large culture dish will do) with sufficient spacers (built-up with tape as in Extended Data Fig. 1d iv) at either end of the slides. When cured, the NOA73 templates are pried from the plastic, and the PDMS wave films on the templates are carefully peeled off and attached to a 24×24 mm cover-glass ready for ECM coating (Extended Data Fig. 1d v).

The above microfabrication procedure was successfully applied to glass rods with diameters down to 100 μm. We were unable, however, to commercially acquire glass rods of smaller diameter to test the lower dimensional limit of our method. In view of this, we developed an augmentative procedure to accomplish wave structure with half periods smaller than that achievable by 100 μm rods. Specifically, drawing inspiration from traditional noodle-pulling, silicone moulds are stretched lengthwise to obtain narrower waves. The stretched moulds are typically fixed in place on a rigid platform with document clips at both ends (Extended Data Fig. 2a). NOA73 is then used to replicate the stretched mould. We have found that, to obtain smoother surfaces, this procedure is best performed over several iterations with small stretch increments each time. And at each iteration, a new silicone mould is produced, from the new narrower wave NOA73 templates, for use in the subsequent stretch

iteration (Extended Data Fig. 2b). It should also be noted that, rather than using PDMS, silicone elastomers with larger elongation at breakage should be used. In our fabrication, Wirosil with a 250 % elongation at break is employed. Furthermore, only a 30 % elongation to the mould is applied at each iteration. This should derive periodic wave structures with half periods of ∼50 μm after 4 iterations—assuming a 0.5 Poisson ratio.

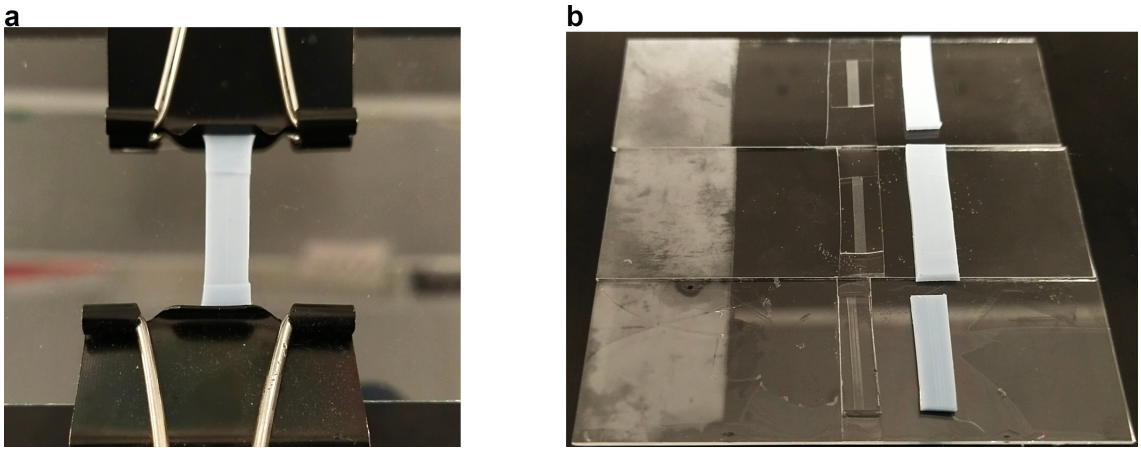

Extended Data Figure 2: **Demonstration of achieving dimensions smaller than commercially available glass rods using a iterative stretching and moulding method. a**, a stretchy silicone with wave pattern is held stretched for optical curable resin casting. **b**, a subsequent stretchy silicone is moulded against the new resin template created from **a**; the whole process is repeated until the desired reduction in dimension is reached.

Using the above methods together, wave structures with half periods of ∼200, ∼100, and ∼50 μm were fabricated (Main-Text Fig. 1a-c, respectively). Rectangular waves of similar periodicity to the cylindrical waves were also produced for comparative studies. These structures were fabricated using standard photolithography and soft-lithography [25].

The surface properties of the PDMS wave substrates, as shown in main-text figure 1a-c, were characterised using a scanning electron microscope (JEOL JSM 6010LV). Meanwhile, to characterise the dimensions of the structures, cylindrical or rectangular, FITC-collagen I from bovine skin (C4361, Sigma-Aldrich) was coated on some of the samples and then imaged on a confocal microscope (see next section). Extended data figures 3a-c show orthogonal fluorescence sections of the ∼50, ∼100, and ∼200 μm cylindrical waves, respectively; while extended data figures 3d-f show that of the rectangular waves. Using FIJI and its kappa plugin, the typical dimensions and curvatures (Extended Data Fig. 3g-h) as determined from the FITC signals are tabulated in extended data figure 4.

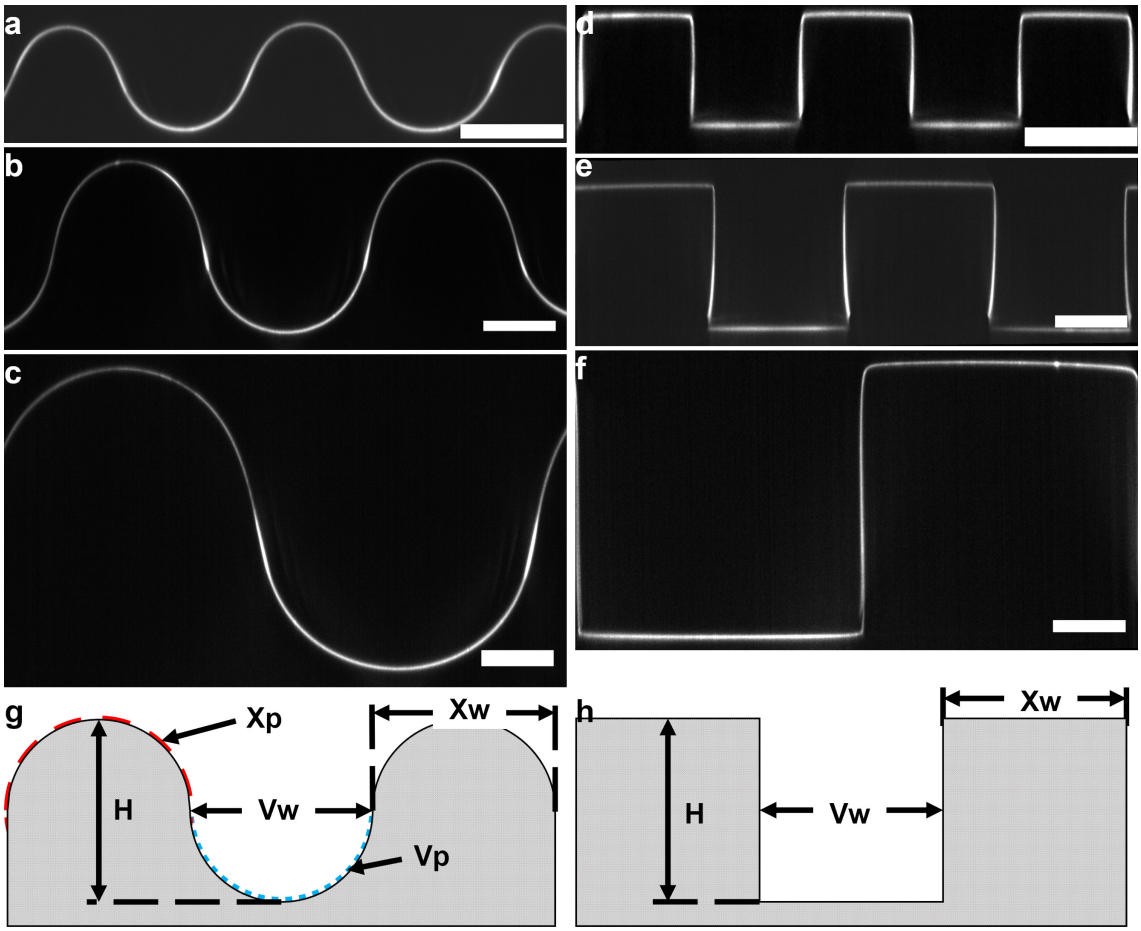

Extended Data Figure 3: **Dimensional characterisation of cylindrical and rectangular waves through fluorescent collagen I z-stacks. a-c**, 50, 100, and 200 μm cylindrical waves. **d-f**, 50, 100, 200 μm rectangular waves. Scale-bars = 50 μm. **g,h**, dimensions measured: curvature (Xp and Vp); width (Xw and Vw); and height (H). Values tabulated in extended data figure 4.

Substrate type	**Profile curvature (mean +/- SD μm^{-1})**	**Curvature variance (mean +/- SD μm^{-2})**	**Profile width (mean +/- SD μm)**	**Total height (mean +/- SD μm)**
50_cyl (concave region)	0.0306 +/- 0.0016	0.0163 +/- 0.0010	63.6 +/- 3.4	53.5 +/- 5.1
50_cyl (convex region)	0.0362 +/- 0.0028	0.0218 +/- 0.0019	49.5 +/- 3.3	
100_cyl (concave region)	0.0173 +/- 0.0003	0.0092 +/- 0.0008	112.1 +/- 0.8	119.0 +/- 0.4
100_cyl (convex region)	0.0174 +/- 0.0011	0.0102 +/- 0.0020	104.9 +/- 0.6	
200_cyl (concave region)	0.0107 +/- 0.0005	0.0071 +/- 0.0008	197.6 +/- 4.6	209.3 +/- 3.4
200_cyl (convex region)	0.0105 +/- 0.0008	0.0068 +/- 0.0011	190.7 +/- 3.4	
50_rec (groove)	-	-	47.1 +/- 1.2	43.0 +/- 1.6
50_rec (ridge)	-	-	47.5 +/- 0.4	
100_rec (groove)	-	-	97.4 +/- 1.1	97.3 +/- 4.3
100_rec (ridge)	-	-	101.8 +/- 2.2	
200_rec (groove)	-	-	190.8 +/- 1.4	187.3 +/- 0.7
200_rec (ridge)	-	-	193.2 +/- 2.4	
For comparison, curvatures of 50 , 100, and 200 μm circles are 0.04, 0.02, and 0.01 μm^{-1} respectively				

Extended Data Figure 4: **Table of cylindrical and rectangular wave dimensions.**

Group	Sample 1	Mean	Std	Sample 2	Mean	Std	Difference	DOF	Welch T	p-value	95% Cohen D
Wave 50	Valley	0.325	0.082	Hill	0.187	0.067	0.138	44.2	6.374	9.372×10^{-8}	[1.144, 2.348]
Wave 100	Valley	0.308	0.094	Hill	0.206	0.071	0.103	35.5	3.893	4.187×10^{-4}	[0.360, 1.857]
Wave 200	Valley	0.195	0.099	Hill	0.213	0.111	-0.018	45.3	-0.586	5.605×10^{-1}	-
Rec 50	Valley	0.359	0.114	Hill	0.418	0.132	-0.059	56.8	-1.852	6.922×10^{-2}	-
Rec 100	Valley	0.295	0.041	Hill	0.226	0.066	0.069	38.5	4.364	9.274×10^{-5}	[0.627, 1.739]
Rec 200	Valley	0.282	0.099	Hill	0.270	0.184	0.012	44.5	0.306	7.607×10^{-1}	-

Extended Data Figure 5: **Post hoc t-test statistics for the comparisons made with regard to the different size of structures.**

Group	Sample 1	Mean	Std	Sample 2	Mean	Std	Difference	DOF	Welch T	Adj. p value	95% Cohen D
Hill	Control	0.267	0.120	Sucrose	0.134	0.067	0.133	55.8	5.758	5.037×10^{-7}	[0.961, 1.867]
				DMSO	0.119	0.073	0.148	59.1	6.075	1.939×10^{-7}	[1.000, 2.004]
				NaCl	0.141	0.072	0.126	58.5	5.213	2.536×10^{-6}	[0.787, 1.808]
				Water	0.470	0.093	-0.203	56.6	-7.383	3.058×10^{-9}	[-1.384, -2.513]
Valley	Control	0.361	0.077	Sucrose	0.117	0.051	0.243	60.8	15.572	1.395×10^{-22}	[3.102, 4.635]
				DMSO	0.090	0.055	0.271	61.6	6.344	1.821×10^{-23}	[3.213, 5.112]
				NaCl	0.165	0.045	0.196	57.7	12.694	3.210×10^{-18}	[2.446, 3.866]
				Water	0.389	0.064	-0.029	55.2	-1.558	1.248×10^{-1}	-
Flat	Control	0.273	0.066	Sucrose	0.115	0.065	0.158	36.0	7.504	2.895×10^{-8}	[1.846, 3.352]
				DMSO	0.137	0.070	0.136	27.3	5.611	5.762×10^{-6}	[1.316, 3.104]
				NaCl	0.162	0.048	0.111	29.9	5.497	5.762×10^{-6}	[1.319, 2.780]
				Water	0.457	0.065	-0.184	24.0	-7.527	1.838×10^{-7}	[-1.864, -4.412]
Control	Hill	0.267	0.120	Flat	0.273	0.066	-0.007	51.4	-0.262	7.940×10^{-1}	-
Control	Valley	0.361	0.077	Flat	0.273	0.066	0.087	39.4	4.313	3.139×10^{-4}	[0.656, 1.863]
Control	Valley	0.361	0.077	Hill	0.267	0.120	0.094	59.9	3.945	3.174×10^{-4}	[0.458, 1.499]
Water	Hill	0.470	0.093	Flat	0.457	0.065	0.013	30.0	0.495	6.241×10^{-1}	-
Water	Valley	0.389	0.064	Flat	0.457	0.065	-0.068	21.9	-2.954	1.104×10^{-2}	[-0.327, -2.069]
Water	Valley	0.389	0.064	Hill	0.470	0.093	-0.081	40.9	-3.506	3.356×10^{-3}	[-0.539, -1.590]

Extended Data Figure 6: **Post hoc t-test statistics for the comparisons made with regard to the different media osmolarities.**

Group	Sample 1	Mean	Std	Sample 2	Mean	Std	Difference	DOF	Welch T	Adj. p value	95% Cohen D
Hill	FAKI14	0.217	0.051	Sucrose	0.134	0.067	0.083	54.9	5.335	3.724×10^{-6}	[0.896, 1.983
				Control	0.267	0.120	-0.050	50.7	-2.227	3.040×10^{-2}	[-0.078, -0.973]
Valley	FAKI14	0.400	0.124	Sucrose	0.117	0.051	0.283	17.5	8.761	1.679×10^{-7}	[2.709, 4.795]
				Control	0.361	0.077	0.040	20.4	1.177	2.529×10^{-1}	-
Flat	FAKI14	0.280	0.073	Sucrose	0.115	0.065	0.165	43.0	7.970	1.051×10^{-9}	[1.718, 3.374]
				Control	0.273	0.066	0.006	38.6	0.292	7.715×10^{-1}	-
FAKI14	Valley	0.400	0.124	Hill	0.217	0.051	0.183	18.3	5.603	2.393×10^{-5}	[1.467, 3.190]

Extended Data Figure 7: **Post hoc t-test statistics for the comparisons made with regard to the FAKI14 treatment.**

Cell culture, staining and imaging

Mardin Darby Canine Kidney type II cells (MTOX1300, ECACC collection purchased from Sigma-Aldrich) were cultured in Minimum Essential Medium (MEM, 11090081, Gibco) supplemented with 5 % FBS (10082147, Gibco), 1× Penicillin/streptomycin (15070063, Gibco), 1× GlutaMax, 1× Sodium Pyruvate (11360070, Gibco), and 1× Non-essential amino acids (11140050, Gibco). The cell line was maintained at 37 °C and 5 % CO_2, and subcultured every other day. Cells are typically disposed of before 25 passages.

In order for cells to attach to the PDMS wave substrates, an extracellular matrix coating is required on the surface. This is done by first activating the surface under oxygen plasma for 3 minutes. Then, 500 μl of 20 mM acetic acid solution containing 50 μg of collagen-I from bovine skin (C4243, Sigma-Aldrich) was added to the substrate supported on a 22×22 mm cover-glass and left for 2 hours at room temperature. After this, the collagen-I solution was aspirated and the substrate air dried for 1 hour. These coated substrates are then stored in 4 °C and typically used within a week. Prior to experimentation, coated substrates are re-immersed in 1× phosphate buffered saline (PBS, P4417, Sigma-Aldrich) in a 35 mm culture dish and UV sterilised for 15 minutes in a biosafety cabinet.

To study MDCK responses over the curved substrates, cells were first re-suspended in imaging media (MEM without phenol red, above supplements and 2 % serum) followed by seeding on to the substrates at a density of $\sim 2.5\times10^5$ cells/cm^2. A figure of eight motion is applied to the sample dish to ensure an even distribution of cells. Live-cell microscopy experiments are performed 24 hours after seeding to ensure closure of the monolayer. Otherwise, the monolayers are fixed, at 24, 48 and 72 hours after seeding, for fluorescence imaging.

For nuclei staining, monolayers reaching desired time-points were rinsed in 1× PBS followed by fixing in 4 % formaldehyde (28906, Thermo Scientific) for 15 minutes. After two 1× PBS washes, the cells are permeabilized with 0.1 % Triton X-100 (X100, Sigma-Aldrich) for 3 minutes. The cells are then twice washed with 1× PBS Cells again, and stained with Hoechst 33342 (H3570, Invitrogen) at 1:1000 dilution. For immunostaining of FAK (610088, BD Transduction Laboratories) and activated FAK (Tyr 397) (AF3398, Affinity Biosciences), after permeablization, cells were first blocked for 30 minutes in 2 % BSA in 1× PBS. The primary antibodies are then diluted 1:400 in the blocking buffer and added to the samples for 2 hours. Afterwards, the samples were rinsed twice in 1× PBS. Secondary antibodies, Alexa Fluor 488 goat anti-rabbit and Alexa Fluor goat anti-mouse (A11008 and A11004, Invitrogen), diluted to 1:400 were then added to the samples and left for another

hour. Stained samples are then washed twice in 1× PBS and left in 1× PBS in 4 °C and imaged within a week.

To perform live-cell microscopy, MDCK monolayer substrates supported on cover-glasses were transferred to a stainless steel cover-glass holder (SC15022, Aireka Scientific, HK) and replaced with fresh image media. The samples are imaged on a Nikon Biostation IMQ, with the cells maintained at 37 °C and 5 % CO_2 through the built-in environmental chamber. Phase contrast z-stack images—13 z-planes for all dimensional conditions—are typically acquired every 7 minutes over 24 hours using the internal 10× objective (0.5 NA) and 1.3-megapixel monochrome camera. Furthermore, to obtain a large field of view, a 3-by-5 overlapping image array is tracked for every time-lapse acquisition.

For imaging fixed and stained samples, these are typically mounted upside down, propped up by spacers, in 1× PBS on cover-glasses, and placed in the same stainless steel cover-glass holder (SC15022, Aireka Scientific, HK) used for live-cell imaging. Fluorescence imaging was then performed on a spinning-disk confocal microscope. Specifically, a Yokogawa CSU-W1 (Yokogawa Electric, Japan) scanner unit attached to a Nikon Ti2-E inverted microscope (Nikon Instruments Inc., US). Fluorophores were excited through a laser module (iLAS laser launcher, Gataca Systems, France) containing 405, 488, 561, 642 nm laser lines. Image z-stacks (z-steps=0.3 μm) were imaged with a 40× water immersion objective (CFI Apo LWD 40XWI λS N.A. 1.15, Nikon) and captured with a sCMOS Camera (Prime 95B 22 mm, Teledyne Photometrics, US). The z-positions were precisely controlled by a piezo stage (PI PIFOC Z-stage, Physik Instrumente, US). The whole microscopy system was controlled by the MetaMorph advanced acquisition software (Molecular Devices, USA).

In order to demonstrate the accumulation of water at the basal side of an epithelial monolayer, MDCK monolayers on glass were transfered to stainless steel culture vessels after 24 hours. However, instead of replenishing with the Iso-osmotic image media described previously, a hyper-osmotic MEM with sucrose is used. Moreover, as the samples will be tightly sealed to prevent osmolarity shifts due to evaporation, MEM with Hank's balanced salt was adopted as the base medium here (11575032, Gibco). After conditioning the cells in hyper-osmotic medium for 4 hours at 37 °C, an air-tight lid is placed on the sample holder and reflection interference contrast microscopy (RICM) was performed in order to track cell-to-substrate attachment over a 5 hour period, with an iso-osmolarity rescue (adding water) performed halfway. RICM was done on a Nikon A1R laser scanning confocal microscope operating in reflection mode using 640 laser excitation. The whole system was maintained

at 37 °C. Hardware autofocus was activated to account for stage drift over time. Furthermore, to ensure the data always contained the reflection plane of interest, z-stacks with a 4 μm range and 200 nm intervals were typically acquired.

RICM was also employed to highlight the difference between cell-to-basal attachments between MDCK monolayers on the hills and valleys of the wave substrates. However, rather than PDMS, the cells were cultured on wave substrates made from the higher refractive index NOA73. The latter is to improve the RICM contrasts. This time, the cells after 24 hours were replenished with iso-osmotic image medium with Hank's balanced salt, and similarly conditioned for 4 hours prior to imaging. Due to the large vertical span of the structures, the features (hill, valley, and flat) were imaged separately. Typically, z-stacks were acquired with a 20 μm range and 200 nm intervals around the apex of geometries (applicable to hills and valleys only). This choice is because RICM fails in regions where the surfaces become vertical.

Osmolarity perturbation, drug treatment, and apoptosis detection

To create hyper-osmotic conditions, 1 % DMSO, 4.1 wt. % sucrose, and 0.4 wt. % NaCl were added to the image media described in the previous section. Meanwhile, a hypo-osmotic condition is created by adding an extra 25 % Milli-Q water. These perturbations amounted to a change in osmolarity (osmolality measured using Vapro vapor pressure osmometer 5520, Wescor Inc., USA) to 418.6 ± 3.5, 403.6 ± 3.8, 406.3 ± 1.5 and 214.6 ± 4.0 mOsm/L (mean ± SD, n = 3), from 279.3 ± 3.8 mOsm/L in control. To test whether inhibiting focal adhesion phosphorylation at tyrosine 397 was sufficient in rescuing cell extrusion rates in MDCK monolayers in hyper-osmotic conditions, image medium containing sucrose was added with 3 μM FAK inhibitor 14 (SML0837-10MG, Sigma-Aldrich) (from 10 mM stock in water) and replaced iso-osmotic media prior to imaging. CellEvent™ (R37111, Invitrogen), a caspase 3/7 substrate that produces fluorescence upon caspase 3/7 activation, was employed to visualize the apoptotic proportion of cell extrusions observed in this study. One drop of the reagent was added to 500 μL of medium one hour before live-cell imaging. To minimize phototoxic effects, only four regions, each with 3 z-steps, were imaged for each sample.

Analysis of extrusion rates

To facilitate the downstream analysis, the 3D image stacks were unwrapped to obtain a 2D representation of the monolayer. To achieve this, the side profiles of

the wave structures were drawn manually. A coordinate map, which detailed the correspondence of the coordinates in 3D space to the 2D plane, was generated from the side profiles. This was then used to unwrap the 3D image stack via spline interpolation.

An attention gated residual U-net was trained to detect extrusion events (Extended Data Fig. 8a). The backbone of the encoder and decoder arms of the network followed that laid out previously in [26] with the following modifications. The residual block was modified using the ResNet-D block [27] with pre-activation [28] and the addition of the Squeeze-and-Excitation block [29]. Furthermore, spatial attention gates were used on the long connections between residual blocks [30]. Due to the inherent class imbalance between the background pixels and the pixels corresponding to the extrusion events, the symmetric unified focal loss was used [31]. Deep-supervision was performed for the various image scales by adding a 1×1 convolution block after each group of residual blocks [32]. The ground truth was downscaled to the appropriate size and the same loss function as the full sized ground truth was used. Spatially varying labelling smoothing was applied to the ground truth image as well as every deep-supervision level to mitigate overconfidence in the network [33].

Training of the network was performed for a total of 200000 training steps with each step having a batch size of 32. The initial number of filters was set at 64. A cosine learning rate decay, which started from an initial learning rate of 5×10^{-4} and decayed to a minimum of 1×10^{-6}, was employed as suggested in [34]. The training data consist of input images with 5 frames, 2 before and 2 after the frame of interest, along with hand annotated mask of the extrusion events (Extended Data Fig. 8b). The intensity of the input images were normalized using percentile normalization. These images were initially 192×192 pixels^2 in size and were subsequently cropped to the final size of 128×128 pixels^2 after data augmentation. Both positive and negative examples were annotated to ensure that only extrusion events were being identified by the network. The following data augmentation were used – flips (horizontal and vertical), transpositions and random rotations (multiples of 90°).

As the extrusion process can occur over a few frames, further downstream processing was done to identify the start of the extrusion event. First, a size filter was used to filter out any small objects smaller than 80 pixel^2. Holes smaller than 80 pixel^2 were filled as well. Objects with an eccentricity > 0.95 and solidity > 0.5 are also removed. Next, the centroid locations of all the objects were calculated. Objects in different frames were determined to belong to the same extrusion event if the distance between the two centroids were less than 20 pixels and the time difference was less than 5 frames. The first instance of the object in each event was used to

represent the position and time of the extrusion. Last, only extrusions that occur within the region of interest and the 24 hr time frame were included in the extrusion rate calculation. The normalized extrusion rate was then calculated by dividing the extrusion rate from each image with the initial cell density for that sample.

Estimation of cell density was done using the StarDist network [35]. Briefly, training data was prepared by hand drawing labels for the cells in representative images using Fiji. The images were also pre-processed using a log-contrast filter to normalize the contrast of the images. The following augmentations were used to augment the training data – random rotation (multiples of 90°), transpositions (horizontal and vertical), flip, motion blur, median blur and Gaussian blur. The training data was also randomly cropped to the final size of 256×256 px before being fed into the network. The default parameters for the StarDist network were used with the exception of number of epoch and iterations per epoch which were set to 1000 and 100 respectively. Prediction of new images were done using the network weights that provided the smallest loss value during training. By passing the first frame of the time-lapse through the network, the number of cells, and consequently the cell density, were determined for each predefined region of interest (Extended Data Fig. 8d). The average initial cell density was then calculated for each sample.

Statistically analysis of the normalized extrusion rate was performed using the Python `statsmodels` module. Two way ANOVA was performed using the type III sums of squares as well as the HC3 heteroskedasticity-consistent standard error estimator. If the interaction term was significant, the main effects were ignored and only the simple main effects were considered. One way ANOVA of the simple main effects was then performed if multiple comparison were made during post hoc testing. Two-tailed Welch's unequal variances T-test were conducted to determine if any of the comparisons were significant. The Benjamini-Hochberg procedure was performed if multiple comparison were made. Normality of the data was verified via visual inspection of the Q-Q plot and histogram of the residuals.

3D force microscopy

To study the forces generated by the cells grown on the curved substrates, polyacrylamide substrates with fluorescent beads evenly dispersed throughout the substrate were fabricated (Extended Data Fig. 9a, d). Specifically, an aliquot of 10 μl of 0.2 μm fluorescent (580/605) carboxylated microspheres (F8810, Invitrogen) was added to 9.5 ml of Milli-Q water and sonicated for 10 minutes. This solution was then filtered using a 0.45 μm syringe filter (Sartorius). A further 0.5 ml of 500 mM of MES buffer, pH 6.0, was added to the filtered solution. A master polyacrylamide mix

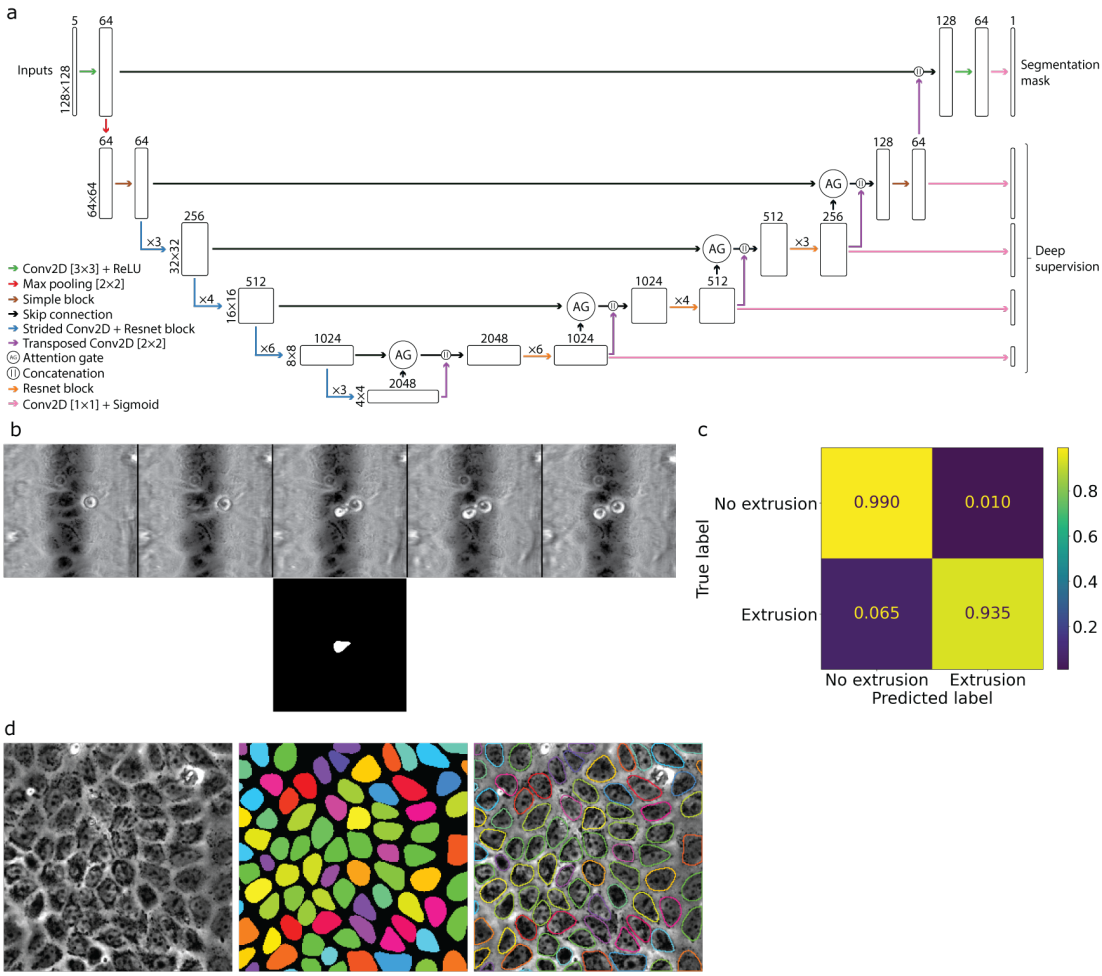

Extended Data Figure 8: **Calculation of the normalized extrusion rate a**, architecture of the attention-gated residual U-Net. **b**, example of a manually annotated extrusion event using the sequence of 5 time frames above and the mask below. **c** confusion matrix of the machine learning network. **d**, Left – bright-field image; Center – prediction from StarDist; Right – overlay of the prediction outline on the bright-field image

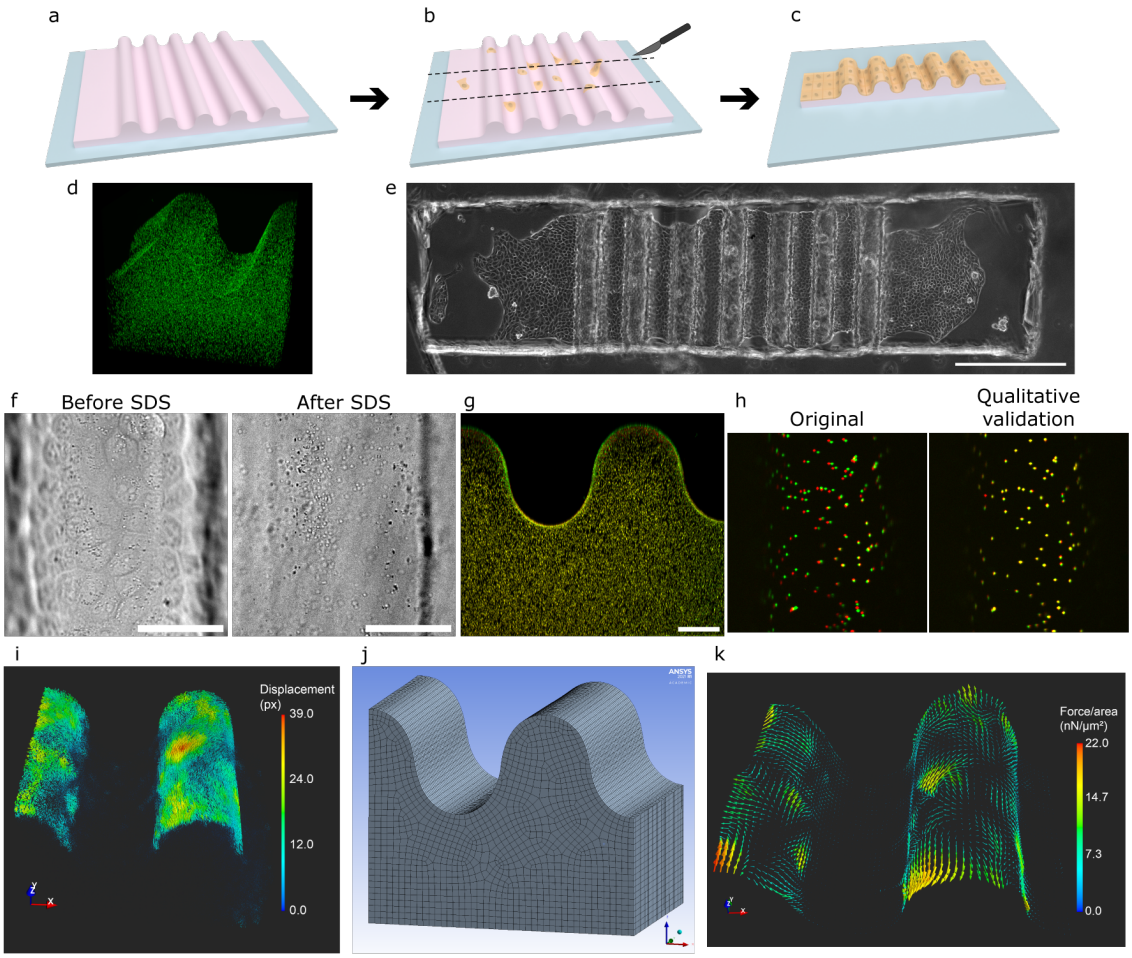

Extended Data Figure 9: **3D force microscopy a-c**, schematic for the preparation of the gel as well as the cell seeding process. **d**, 3D view showing the even distribution of fluorescent beads in the polyacrylamide gel. **e** bright field image showing the cut get and the monolayer of cells on the curved substrate. Scale-bars = 500 μm. **f**, bright field images showing the removal of cells through the addition of 1 % SDS. **g** maximum projected side profile of the polyacrylamide gel before (red) and after SDS treatment (green). **h** Qualitative validation of the calculated displacements. Left – original fluorescent image showing the bead locations with cells (red) and without cells (green). Right – overlay of the mapped image (green) and the bead image with cells (red). **i** 3D view of the calculated displacements obtain using the two-frame 3D farneback optical flow method. **j** Representative 3D structure and mesh used in the finite element modelling of the polyacrylamide structure. **k** 3D view of the average nodal force obtain by solving the inverse problem. Scale-bars = 50 μm unless otherwise stated.

was then generated by mixing 200 μl of 40 % polyacrylamide solution (Bio-Rad), 200 μl of 2 % bis-acrylamide solution, 580 μl of the filtered bead solution and 1.5 μl of TEMED. Next, to 150 μl of the master mix, 2 μl of 10 % APS was added and mixed using a vortex. This was then added onto the NOA73 molds described in the previous sections before a cover-glasses was placed on top of the mold. The polyacrylamide was allowed to gel for 30 minutes. To ensure that the polyacrylamide gel binds to the cover-glasses, the cover-glasses were previously treated with a solution containing 2 % trimethoxysilyl propyl methacrylate (Sigma-Aldrich) and 1 % glacial acetic acid in absolute ethanol for 10 minutes. The cover-glasses were then washed 3 $\times$ in absolute ethanol before being dried in an oven at 80 °C for 2 hours. The mold was then separated from the glass cover-glasses and the polyacrylamide gel. This process was done under PBS to ensure that the polyacrylamide gel separates cleanly. The polyacrylamide gel was subsequently washed 3 $\times$ with PBS before being stored in PBS at 4 °C overnight.

To allow for the MDCK cells to attach to the polyacrylamide gel, the surface was coated with collagen-I from bovine skin (C4243, Sigma-Aldrich). This was achieved by functionalizing the gel surface using sulfosuccinimidyl 6-(4'-azido-2'-nitrophenylamino)hexanoate (sulfo-SANPAH). Specifically, 40 μl of 0.2 % acetic acid was added to 2 μl of 0.02 mg/ml sulfo-SANPAH that had been previously dissolved in DMSO. This solution was then added to the polyacrylamide gel surface. A silicone block was used to mechanically agitate the solution to ensure even distribution of the sulfo-SANPAH. UV treatment of the sulfo-SANPAH was done using a UV-KUB 9 (Kloe) at 6 % power for 5 minutes. The gel was then washed 3 $\times$ in 0.2 % acetic acid. This process was repeated a second time with fresh sulfo-SANPAH. Finally, the gel was washed 3 $\times$ with PBS. 400 μl of PBS containing 50 μg of collagen-I was aspirated onto the gel surface. The collagen was left for 2 hours at room temperature with occasional mixing with a pipette to prevent any collagen gel formation. The gel was then washed 3 $\times$ with PBS before being stored in PBS. Cell seeding was performed as described previously. After the cell have initially started to attached, the gel was cut using a sharp blade until a small region of interest of approximately 5$\times$1 mm is left (Extended Data Fig. 9b). The cells were then allowed to grow for 24 hours until a full monolayer was formed (Extended Data Fig. 9c, e).

To image the bead displacements, the gel containing cover-glasses were transferred to a stainless steel cell culture vessels and 500 μl of the original media, in which the cell were previously growing in, were added. The vessels were sealed using a custom-made lid to ensure proper humidity control. Imaging of the beads were done using the same imaging system previously used for fixed cells. A z-step size

of 0.275 μm was used for this imaging to ensure that the voxel size is the same for all dimensions. Two sets of fluorescent bead images were captured. The first set consist of a z-stack of the beads that was captured with the cell still attached to the gel. The second set consisting of a time-lapse of 5 frmaes at 15 minute intervals was captured after the cell were removed using 100 μl of sodium dodecyl sulfate (SDS) solution. The SDS solution was prepared by diluting 10 % SDS using the original media to reach a final concentration of 1 %. To minimize any gel deformation, an additional 250 μl of Milli-Q water was added per 1 ml of SDS solution to minimize any gel volume changes due to the addition of SDS. A representative bright-field image of the cells and projected side profile of the fluorescent beads before and after SDS treatment are shown in Extended Data Fig. 9 f and g respectively.

The displacement of the beads was determined using the two-frame 3D Farneback optical flow method [36]. A CUDA accelerated implementation was written in Python to speed up the computational time required for displacement estimation. The following parameters for the algorithm were used – 5 iterations, 5 pyramid levels with a scaling factor of 0.5, kernel size of 7 px and box filter size of 31 px. The images were pre-processed by aligning the two sets of images manually before being smoothed with a Gaussian filter of radius 7 px. Validation of the estimated displacement were done by using the estimated displacements to generate a pixel map. This pixel map was used to map the pixels from the bead image without any cells. Qualitative validation can then be performed by visually inspecting if there are reasonable alignment between this mapped image and the bead image with cells (Extended Data Fig. 9h). Post processing of the estimated vectors were done as followed. First, a suitable region deep in the substrate was chosen and the median x and y displacement from this region was used to eliminate any residual displacement in x and y due to misalignment of the two images. Second, the z displacements along the cross section of the hill were fitted using a best fit line to obtain the z displacement correction function. This function would adjust for any misalignment in z as well as gel shape changes in z as a result of minor changes to the salt concentration. Last, displacements outside the region of interest were set as undefined.

The calculation of forces from the displacements were treated as a linear inverse problem. Here, the output (calculated displacements, Extended Data Fig. 9i) and the system were known, while the input (force exerted by the cells) needed to be computed. The system could be obtained from finite element modelling of the gel. The shape of the gel was obtained by subdividing the image into smaller 3D subsets along the axis perpendicular to the feature. Thresholding was preformed to obtain

the centroid location of the beads in each subsets. The centroid locations were projected along the axis perpendicular to the feature to obtain a representation of the points on a 2D plane. The alpha shape of the 2D plane was then determined and the outlines for the alpha shapes from each subset were used to calculate the 3D representation of the gel using the "Blend" tool in Ansys SpaceClaim 2021 R1. The 3D representation was meshed using Ansys 2012 R1 with the top face having a maximum element edge length of 5.5 μm (Extended Data Fig. 9j). The bottom face was set using the zero displacement boundary condition. To account for any edge effects, the symmetric boundary condition was set for all the faces except for the top and bottom faces. The material properties were specified with a Young's modulus of 30 kPa and a Poisson's ratio of 0.457. For each node on the top surface of the mesh, a nodal force of 1×10^{-8} N was applied to the x, y, and z directions sequentially and the corresponding nodal displacement of all the nodes was then recorded. The nodal displacements were then arranged into a matrix describing the response of the system to various nodal forces. The calculated displacements were also mapped to the various nodal positions to obtain the outputs at each node. The inverse problem was then solved via regularization using the Tikhonov method with the regularization parameter determined using the L-curve method. The surface force per unit area was subsequently calculated by taking the average force of a node and its neighbours and dividing it by the area covered by the nodes (Extended Data Fig. 9k).

Image processing and data analysis

RICM data. Our RICM data comprises of z-stacks taken over time and/or over regions. And using the fact RICM images are brightest when focus falls on the plane of reflection, the reflecting plane at which cells meet the surface were extracted by performing maximum projection in ImageJ (Main-Text Fig. 2e, f and i). Furthermore, from the principles of RICM, focal adhesions, being the closest objects to the substrates, should exhibit the lowest intensities [12, 13]. Utilizing this property, we effectively removed fluctuating backgrounds across time frames by left-shifting the histograms of each frame such that all the minima align at zero. This allowed us to register the changing intensities—i.e., the cell-substrate basal separation—over time more accurately (Main-Text Fig. 2g). Then, to derive a quantitative comparison, the medians of the grey values were averaged over the duration of the treatments (hypo-osmotic or iso-osmotic). Average medians from 3 regions and 3 independent samples were compiled (Main-Text Fig. 2h), and statistical significance calculated using a paired t-test.

On the other hand, to make the intensity comparisons between cells on the flat, hill and valley regions, rectangular ROIs of 12 × 150 μm were first randomly selected from the max-projected z-stacks of each feature. Based on similar reasoning, the histogram minima were left-aligned to zero grey value. To facilitate quantitative comparisons, median grey values were extracted from the aligned histograms—3 ROIs for each feature, and from 4 independent samples (Main-Text Fig. 2j). A student's t-test was used to calculate the significance.

FAK phosphorylation. Due to the 3D nature of our wave substrates, differences in the raw intensities of phosphorylated focal adhesion kinase (pFAK) fluorescence between hill and valley cells cannot, by itself, be used as the proxy for the actual differences. We needed to first eliminate differences contributed by optical scattering through the material, and variations in staining. To achieve this, we first normalized hill and valley pFAK and total FAK median grey values against the average median values obtained from 3 random flat regions of the same sample. Then, the ratios, pFAK/FAK, from 3 regions and 3 independent samples were calculated and compiled (Main-Text Fig. 4e). A student's t-test was used to calculate the significance in the relative activation of pFAK between cells on the hills and those in the valleys.

All Data analysis in this section was performed using the statistical programming software, R. The graphs were prepared using the ggplot2 package.

Immunoblot Analysis

Preparation of MDCK cell lysates. At the end of experiment time-points, the attaching MDCK cells were collected by trypsinization (TrypLE Express, Thermo Scientific) supplemented with 50 mM EDTA (Thermo Scientific). The cell pellets were then lysed in radioimmune precipitation assay (RIPA) buffer (Thermo Scientific) containing 25 mM Tris-HCl, pH 7.6, 150 mM NaCl, 1 % NP-40, 1 % sodium deoxycholate, 0.1 % sodium dodecyl sulfate (SDS) and added with protease and phosphatase inhibitor cocktail (Halt™, dilution: 1:100, Thermo Scientific). The lysates were centrifuged at 13,000 rpm for 15 mins at 4 °C to separate the cell debris from the protein-rich supernatant. The supernatants were then collected into fresh tubes, and protein concentrations were determined by bicinchoninic acid (BCA) assay kit (Thermo Scientific) as per manufacturer's instructions.

Immunoblotting. Protein samples were added with equal volume of 2× Laemmli sample buffer (Bio-Rad Laboratories, Hercules, CA, USA) containing 65.8 mM Tris-HCl, pH 6.8, 2.1 % SDS, 26.3 % (w/v) glycerol, 0.01 % bromophenol blue and supplemented with 200 mM dithiothreitol (DTT, Merck). The resultant

mixtures were then denatured at 95 °C for 7 minutes and cooled to room temperature. The denatured protein samples (20 μg) were then separated on 4-20 % SDS-polyacrylamide gels using a Tris-glycine running buffer (Bio-Rad) and electroblotted onto nitrocellulose membranes (0.2 μm pore size, Bio-Rad) using a wet Criterion blotter (Bio-Rad) in transfer buffer containing 25 mM Tris base, 150 mM glycine, and 20 % (v/v) methanol for 1 hr at 100 V. The membranes were then incubated in blocking buffer, consists of 5 % (w/v) bovine serum albumin (BSA, Hyclone) in Tris-buffered saline (1× TBST, containing 20 mM Tris-HCl, pH 7.5, 137 mM NaCl and 0.2 % Tween-20) for 1 hr at room temperature to minimize non-specific binding. The membranes were then incubated for 24-48 hr at 4 °C in antibodies targeting the following proteins (dilution factors, incubation duration and manufacturer's catalogue numbers are tabulated in Extended Data Fig. 10): FAK, phosphorylated-FAK (Tyr397), Pan-AKT, phosphorylated-AKT (Ser473) and GAPDH diluted in blocking buffer. After three washes with 1× TBST, the membranes were incubated in either horseradish peroxidase (HRP)-conjugated goat anti-rabbit IgG (dilution: 1:3000, CST cat# 7074) or horse anti-mouse IgG (dilution factor 1:3000, CST cat# 7076) diluted in blocking buffer for 1 hr at room temperature. The membranes were then subjected to peroxidase-based detection by using enhanced chemiluminescence (ECL) detection reagent (Clarity Max™ Western ECL Substrate, Bio-Rad), and the chemiluminescent signals were visualized by ChemiDoc Touch System (Bio-Rad) and captured by Image Lab software (v 5.2.1). Protein levels were quantified by densitometric analysis using ImageJ software (v 1.53o, National Institute of Health, USA). **Statistical analysis.** Numerical values

Target	Host	Type	Dilution	Incubation Time (h)	Manufacturer	Cat. No.
AKT (pan)	Rabbit	Monoclonal	1:1000	24	CST	4691
Phospho-AKT (Ser473)	Rabbit	Monoclonal	1:1000	48	CST	4060
FAK	Mouse	Monoclonal	1:500	48	BD Biosciences	611008
Phospho-FAK (Try397)	Rabbit	Monoclonal	1:1000	48	Thermo Scientific	700255
GAPDH	Mouse	Monoclonal	1:1000	24	Santa-Cruz Biotech	32233

Extended Data Figure 10: **Dilution factors, incubation duration and manufacturer's catalogue numbers for immunoblotting.**

are expressed as mean ± SD. Statistical analyses of all data were performed using two-tailed Student's t-test to determine the differences between treatment groups and control group. P values which are less than 0.05 are considered significant in all

statistical analyses, where * depicts $P < 0.05$, **$P < 0.01$, ***$P < 0.001$, ****$P < 0.0001$. All statistical analyses were performed using GraphPad Prism software (v 6.01, GraphPad Software, Inc, La Jolla, CA, USA).

References

[1] Shizue Ohsawa, John Vaughen, and Tatsushi Igaki. Cell Extrusion: A Stress-Responsive Force for Good or Evil in Epithelial Homeostasis. *Developmental Cell*, 44(3):284–296, 2018.

[2] Lance W. Peterson and David Artis. Intestinal epithelial cells: Regulators of barrier function and immune homeostasis. *Nature Reviews Immunology*, 14(3):141–153, 2014.

[3] Gloria Slattum, Karen M. McGee, and Jody Rosenblatt. P115 RhoGEF and microtubules decide the direction apoptotic cells extrude from an epithelium. *Journal of Cell Biology*, 186(5):693–702, 2009.

[4] Takanori Chiba, Erika Ishihara, Norio Miyamura, Rika Narumi, Mihoko Kajita, Yasuyuki Fujita, Akira Suzuki, Yoshihiro Ogawa, and Hiroshi Nishina. MDCK cells expressing constitutively active Yes-associated protein (YAP) undergo apical extrusion depending on neighboring cell status. *Scientific Reports*, 6(January):1–10, 2016.

[5] Yapeng Gu, Jill Shea, Gloria Slattum, Matthew A Firpo, Margaret Alexander, Sean J Mulvihill, Vita M Golubovskaya, and Jody Rosenblatt. Defective apical extrusion signaling contributes to aggressive tumor hallmarks. *eLife*, 4:e04069, 2015.

[6] George T. Eisenhoffer, Patrick D. Loftus, Masaaki Yoshigi, Hideo Otsuna, Chi Bin Chien, Paul A. Morcos, and Jody Rosenblatt. Crowding induces live cell extrusion to maintain homeostatic cell numbers in epithelia. *Nature*, 484(7395):546–549, 2012.

[7] Laurens G. Van Der Flier and Hans Clevers. Stem cells, self-renewal, and differentiation in the intestinal epithelium. *Annual Review of Physiology*, 71:241–260, 2009.

[8] Denis Krndija, Fatima El Marjou, Boris Guirao, Sophie Richon, Olivier Leroy, Yohanns Bellaiche, Edouard Hannezo, and Danijela Matic Vignjevic. Active

cell migration is critical for steady-state epithelial turnover in the gut. *Science*, 365(6454):705–710, 8 2019.

[9] Sebastien J.P. Callens, Rafael J.C. Uyttendaele, Lidy E. Fratila-Apachitei, and Amir A. Zadpoor. Substrate curvature as a cue to guide spatiotemporal cell and tissue organization. *Biomaterials*, 232(September 2019):119739, 2020.

[10] Kenneth R Spring. Epithelial Fluid Transport—A Century of Investigation. *Physiology*, 14(3):92–98, 6 1999.

[11] Nabil A. Abaza, Joseph Leighton, and Stanley G. Schultz. Effects of ouabain on the function and structure of a cell line (MDCK) derived from canine kidney: I. Light microscopic observations of monolayer growth. *In Vitro: Journal of the Tissue Culture Association*, 10(3):172–183, 1974.

[12] A S G Curtis. THE MECHANISM OF ADHESION OF CELLS TO GLASS : A Study by Interference Reflection Microscopy. *Journal of Cell Biology*, 20(2):199–215, 2 1964.

[13] J P Heath and G A Dunn. Cell to substratum contacts of chick fibroblasts and their relation to the microfilament system. A correlated interference-reflexion and high-voltage electron-microscope study. *Journal of cell science*, 29(1):197–212, 1978.

[14] Laurent Limozin and Kheya Sengupta. Quantitative Reflection Interference Contrast Microscopy (RICM) in Soft Matter and Cell Adhesion. *ChemPhysChem*, 10(16):2752–2768, 11 2009.

[15] Xianbin Yong, Cheng-Kuang Huang, and Chwee Teck Lim. An integrated platform to facilitate the calculation, validation and visualization of optical flow velocities in biological images. *Journal of The Royal Society Interface*, 18(179):20210248, 2 2022.

[16] Cheng Kuang Huang, Giovanni J. Paylaga, Sasinan Bupphathong, and Keng Hui Lin. Spherical microwell arrays for studying single cells and microtissues in 3D confinement. *Biofabrication*, 12(2), 2020.

[17] Kenry, Man Chun Leong, Mui Hoon Nai, Fook Chiong Cheong, and Chwee Teck Lim. Viscoelastic Effects of Silicone Gels at the Micro- and Nanoscale. *Procedia IUTAM*, 12:20–30, 2015.

[18] Peter J Reddig and Rudy L Juliano. Clinging to life: cell to matrix adhesion and cell survival. *Cancer and Metastasis Reviews*, 24(3):425–439, 2005.

[19] Steven K Hanks, Larisa Ryzhova, Nah-Young Shin, and Jan Brábek. Focal adhesion kinase signaling activities and their implications in the control of cell survival and motility. *Frontiers in Bioscience-Landmark*, 8(4):982–996, 2003.

[20] Yoshio Terada, Seiji Inoshita, Satoko Hanada, Haruko Shimamura, Michio Kuwahara, Wataru Ogawa, Masato Kasuga, Sei Sasaki, and Fumiaki Marumo. Hyperosmolality activates Akt and regulates apoptosis in renal tubular cells. *Kidney International*, 60(2):553–567, 2001.

[21] Amy E. Shyer, Tyler R. Huycke, Changhee Lee, L. Mahadevan, and Clifford J. Tabin. Bending Gradients: How the intestinal stem cell gets its home. *Cell*, 161(3):569–580, 2015.

[22] Marine Luciano, Shi Lei Xue, Winnok H. De Vos, Lorena Redondo-Morata, Mathieu Surin, Frank Lafont, Edouard Hannezo, and Sylvain Gabriele. Cell monolayers sense curvature by exploiting active mechanics and nuclear mechanoadaptation. *Nature Physics*, 17(12):1382–1390, 2021.

[23] Vahid Hosseini, Philip Kollmannsberger, Samad Ahadian, Serge Ostrovidov, Hirokazu Kaji, Viola Vogel, and Ali Khademhosseini. Fiber-Assisted Molding (FAM) of surfaces with tunable curvature to guide cell alignment and complex tissue architecture. *Small*, 10(23):4851–4857, 2014.

[24] Chenglin Liu, Jiayi Xu, Shijie He, Wanjun Zhang, Huiqi Li, Bo Huo, and Baohua Ji. Collective cell polarization and alignment on curved surfaces. *Journal of the Mechanical Behavior of Biomedical Materials*, 88(May):330–339, 2018.

[25] C.-K. Huang and Athene Donald. Revealing the dependence of cell spreading kinetics on its spreading morphology using microcontact printed fibronectin patterns. *Journal of The Royal Society Interface*, 12(102):20141064–20141064, 2014.

[26] Michal Drozdzal, Eugene Vorontsov, Gabriel Chartrand, Samuel Kadoury, and Chris Pal. The Importance of Skip Connections in Biomedical Image Segmentation. In Gustavo Carneiro, Diana Mateus, Loïc Peter, Andrew Bradley, João Manuel R. S. Tavares, Vasileios Belagiannis, João Paulo Papa, Jacinto C. Nascimento, Marco Loog, Zhi Lu, Jaime S. Cardoso, and Julien Cornebise, editors, *Deep Learning and Data Labeling for Medical Applications*, volume 10008, pages 179–187. Springer International Publishing, Cham, 2016.

[27] Tong He, Zhi Zhang, Hang Zhang, Zhongyue Zhang, Junyuan Xie, and Mu Li. Bag of Tricks for Image Classification with Convolutional Neural Networks.

In *2019 IEEE/CVF Conference on Computer Vision and Pattern Recognition (CVPR)*, pages 558–567, Long Beach, CA, USA, June 2019. IEEE.

[28] Kaiming He, Xiangyu Zhang, Shaoqing Ren, and Jian Sun. Identity Mappings in Deep Residual Networks. In Bastian Leibe, Jiri Matas, Nicu Sebe, and Max Welling, editors, *Computer Vision – ECCV 2016*, volume 9908, pages 630–645. Springer International Publishing, Cham, 2016.

[29] Jie Hu, Li Shen, and Gang Sun. Squeeze-and-Excitation Networks. In *2018 IEEE/CVF Conference on Computer Vision and Pattern Recognition*, pages 7132–7141, Salt Lake City, UT, June 2018. IEEE.

[30] Jo Schlemper, Ozan Oktay, Michiel Schaap, Mattias Heinrich, Bernhard Kainz, Ben Glocker, and Daniel Rueckert. Attention gated networks: Learning to leverage salient regions in medical images. *Medical Image Analysis*, 53:197–207, April 2019.

[31] Michael Yeung, Evis Sala, Carola-Bibiane Schönlieb, and Leonardo Rundo. Unified Focal loss: Generalising Dice and cross entropy-based losses to handle class imbalanced medical image segmentation. *Computerized Medical Imaging and Graphics*, 95:102026, January 2022.

[32] Qikui Zhu, Bo Du, Baris Turkbey, Peter L. Choyke, and Pingkun Yan. Deeply-supervised CNN for prostate segmentation. In *2017 International Joint Conference on Neural Networks (IJCNN)*, pages 178–184, Anchorage, AK, USA, May 2017. IEEE.

[33] Mobarakol Islam and Ben Glocker. Spatially Varying Label Smoothing: Capturing Uncertainty from Expert Annotations. In Aasa Feragen, Stefan Sommer, Julia Schnabel, and Mads Nielsen, editors, *Information Processing in Medical Imaging*, volume 12729, pages 677–688. Springer International Publishing, Cham, 2021.

[34] Irwan Bello, William Fedus, Xianzhi Du, Ekin Dogus Cubuk, Aravind Srinivas, Tsung-Yi Lin, Jonathon Shlens, and Barret Zoph. Revisiting resnets: Improved training and scaling strategies. *Advances in Neural Information Processing Systems*, 34, 2021.

[35] Uwe Schmidt, Martin Weigert, Coleman Broaddus, and Gene Myers. Cell Detection with Star-Convex Polygons. In Alejandro F. Frangi, Julia A. Schnabel, Christos Davatzikos, Carlos Alberola-López, and Gabor Fichtinger, editors,

Medical Image Computing and Computer Assisted Intervention – MICCAI 2018, volume 11071, pages 265–273. Springer International Publishing, Cham, 2018.

[36] Gunnar Farnebäck. Two-Frame Motion Estimation Based on Polynomial Expansion. In Gerhard Goos, Juris Hartmanis, Jan van Leeuwen, Josef Bigun, and Tomas Gustavsson, editors, *Image Analysis*, volume 2749, pages 363–370. Springer Berlin Heidelberg, Berlin, Heidelberg, 2003.